

1 **Diagnosing the thickness-weighted averaged eddy-mean**
2 **flow interaction from an eddying North Atlantic**
3 **ensemble, Part I: Kinematic framework**

4 **Takaya Uchida^{1*}, Quentin Jamet¹, William K. Dewar^{1,2}, Julien Le Sommer¹,**
5 **Thierry Penduff¹ & Dhruv Balwada³**

6 ¹Université Grenoble Alpes, CNRS, IRD, Grenoble-INP, Institut des Géosciences de l'Environnement,
7 France

8 ²Department of Earth, Ocean and Atmospheric Science, Florida State University, USA

9 ³Lamont-Doherty Earth Observatory, Columbia University, USA

10 **Key Points:**

- 11 • Eddying ensemble runs of the North Atlantic Ocean are used to diagnose the thickness-
12 weighted averaged eddy-mean flow interaction.
- 13 • A dynamically consistent neutral surface is implemented to define the buoyancy
14 coordinate for a realistic equation of state.
- 15 • The Eliassen-Palm flux convergence tends to meridionally smooth out the Gulf
16 Stream.

*

Corresponding author: Takaya Uchida, takaya.uchida@univ-grenoble-alpes.fr

17 **Abstract**

18 The thickness-weighted average (TWA) framework, which treats the residual-mean flow
 19 as the prognostic variable, provides a clear theoretical formulation of the eddy feedback
 20 onto the residual-mean flow. The averaging operator involved in the TWA framework,
 21 although in theory being an ensemble mean, in practice has often been approximated
 22 by a temporal mean. Here, we analyze an ensemble of North Atlantic simulations at mesoscale-
 23 permitting resolution ($1/12^\circ$). We therefore recognize means and eddies in terms of en-
 24 semble means and fluctuations about those means. The ensemble dimension being or-
 25 thogonal to the temporal and spatial dimensions negates the necessity for an arbitrary
 26 temporal or spatial scale in defining the eddies. Eddy-mean flow feedbacks are encap-
 27 sulated in the Eliassen-Palm (E-P) flux tensor and its convergence indicates that eddy
 28 momentum fluxes dominate in the separated Gulf Stream. The eddies contribute to the
 29 zonal meandering of the Gulf Stream and smoothing of it in the meridional direction by
 30 decelerating the subpolar and subtropical gyres.

31 **Plain Language Summary**

32 We have greatly benefited from global climate simulations in gaining insight into
 33 what the climate would look like in an ever warming future. Due to computational con-
 34 straints, however, the oceanic component of such simulations have been poorly constrained;
 35 the storm systems in the ocean, often referred to as eddies, have the spatial scales of roughly
 36 several tens of kilometers and simulating the currents associated with eddies accurately
 37 on a global scale, which is on the order of thousands of kilometers, has remained chal-
 38 lenging. Although relatively small in scale compared to the global ocean, eddies have been
 39 known to modulate the climate by transporting heat from the equator to the poles. By
 40 running a regional simulation of the North Atlantic Ocean and taking advantage of re-
 41 cent theoretical developments, we implement a new framework to evaluate such simu-
 42 lations.

43 **1 Introduction**

44 Eddy-mean flow interaction has been a key framework in understanding jet forma-
 45 tion in geophysical flows such as in the atmosphere and ocean (Vallis, 2017). A promi-
 46 nent example of such a jet in the North Atlantic ocean is the Gulf Stream. Previous stud-
 47 ies have shown how eddies fluxing buoyancy and momentum back into the mean flow en-
 48 ergize the Gulf Stream (Lévy et al., 2010; Waterman & Lilly, 2015; Chassignet & Xu,

49 2017; Aluie et al., 2018). Basin-scale simulations, however, often lack sufficient spatial
50 resolution to accurately resolve the eddies and hence, result in underestimating the eddy
51 fluxes of momentum and tracers (Capet et al., 2008b; Arbic et al., 2013; Kjellsson & Zanna,
52 2017; Balwada et al., 2018; Uchida et al., 2019; Schubert et al., 2020). Due to compu-
53 tational constraints, we will continue to rely on models which only partially resolve the
54 mesoscale, a scale roughly on the order of $O(20-200 \text{ km})$ at which the ocean currents are
55 most energetic (Stammer, 1997; Xu & Fu, 2011, 2012; Ajayi et al., 2020), for global ocean
56 and climate simulations. As a result, there has been an on-going effort to develop energy-
57 backscattering eddy parametrizations which incorporate the dynamical effects of eddy
58 momentum fluxes due to otherwise unresolved mesoscale turbulence (e.g. Kitsios et al.,
59 2013; Zanna et al., 2017; Berloff, 2018; Bachman et al., 2018; Bachman, 2019; Jansen et
60 al., 2019; Perezhogan, 2019; Zanna & Bolton, 2020; Juricke et al., 2020).

61 There has been less emphasis, however, on quantifying the spatial and temporal
62 characteristics of the eddy buoyancy and momentum fluxes themselves, which the parametriza-
63 tions are deemed to represent. The focus of this study is, therefore, to examine the dy-
64 namical effects of mesoscale turbulence on the mean flow in realistic, partially air-sea cou-
65 pled, eddying ensemble runs of the North Atlantic. The thickness-weighted average (TWA)
66 framework, which treats the residual-mean velocity as a prognostic variable, allows for
67 a straightforward theoretical expression of the eddy feedback onto the residual-mean flow
68 (e.g. Gallimore & Johnson, 1981; Andrews, 1983; de Szoeke & Bennett, 1993; McDougall
69 & McIntosh, 2001; Young, 2012; Maddison & Marshall, 2013; Aoki, 2014). It is well known
70 in the atmospheric and Southern Ocean literature that it is the residual-mean flow, which
71 is the residual that emerges upon the cancellation between the Eulerian mean flow and
72 eddies, that captures the mean flow for heat and tracer transport (Vallis, 2017). The TWA
73 framework has been fruitful in examining eddy-mean flow interaction in idealized mod-
74 elling studies (e.g. D. P. Marshall et al., 2012; Cessi & Wolfe, 2013; Ringler et al., 2017;
75 Bire & Wolfe, 2018). Here, we extend these studies to a realistic simulation of the North
76 Atlantic.

77 To our knowledge, Aiki and Richards (2008), Aoki et al. (2016) and Zhao and Mar-
78 shall (2020) are the only studies that diagnose the TWA framework in realistic ocean sim-
79 ulations. Aiki and Richards (2008), however, recompute the hydrostatic pressure using
80 potential density for their off-line diagnosis in defining their buoyancy coordinate, which
81 can result in significant discrepancies from the pressure field used in their on-line cal-

82 culation and consequently errors in the diagnosed geostrophic shear. Although Aoki et
 83 al. (2016) negate this complication between the buoyancy coordinate and mean pressure
 84 field by analyzing their outputs in geopotential coordinates, they compute the eddy com-
 85 ponent of the pressure term (F^+ in their paper) using potential density, resulting in er-
 86 rors in the interfacial form stress (viz. this violates equation (10) described below for ϕ'
 87 and m'). The usage of geopotential coordinates also results in a truncation of Taylor ex-
 88 pansion about the mean position of buoyancy surfaces, limiting the accuracy of the eddy
 89 terms. Lastly, all three studies assume ergodicity. The ergodic assumption of treating
 90 a temporal mean equivalent to an ensemble mean, although a pragmatic one, prevents
 91 examining the temporal evolution of the residual-mean fields and conflates temporal vari-
 92 ability with the eddies, which can have leading-order consequences in quantifying the en-
 93 ergy cycle. By adjusting the temporal mean from monthly to annual, Aiki and Richards
 94 (2008, cf. Table 2 in their paper) show that the amount of kinetic and potential energy
 95 stored in the mean and eddy reservoirs can change by up to a factor of four. Eddy-mean
 96 flow interaction in the TWA framework, hence, warrants further investigation, and we
 97 believe our study is the first to strictly implement an ensemble mean in this context.

98 When discussing *eddy* versus *mean flow*, one of the ambiguities lies in how the two
 99 are decomposed and interpreted (Bachman et al., 2015). As noted above, often, the ed-
 100 dies are defined from a practical standpoint as the deviation from a temporally and/or
 101 spatially coarse-grained field regardless of the coordinate system (e.g. Aiki & Richards,
 102 2008; Lévy et al., 2012; Sasaki et al., 2014; Griffies et al., 2015; Aoki et al., 2016; Uchida
 103 et al., 2017; Zhao & Marshall, 2020), which leaves open the question of how the filter-
 104 ing affects the decomposition. Due to the ensemble averaging nature of the TWA frame-
 105 work, we are able to uniquely define the two; the *mean flow* (ensemble mean) is the oceanic
 106 response to the surface boundary state and lateral boundary conditions, and the *eddy* (fluc-
 107 tuations about the ensemble mean) is the field due to intrinsic variability including mesoscale
 108 turbulence (Sérazin et al., 2017; Leroux et al., 2018).

109 The paper is organized as follows: We describe the model configuration in section 2
 110 and briefly provide an overview of the TWA framework in section 3. The results are given
 111 in section 4. In particular, our dataset provides a unique opportunity to examine the va-
 112 lidity of the often assumed ergodicity when decomposing the flow into its eddy and mean
 113 flow components, which we give in section 4.2. Discussion and conclusions are given in
 114 section 5.

115 2 Model description

116 We use the model outputs from the realistic runs described in Jamet et al. (2019b)
 117 and Jamet et al. (2020), which are a air-sea partially coupled, 48-member ensemble of
 118 the North Atlantic ocean at mesoscale-permitting resolution ($1/12^\circ$; or sometimes re-
 119 ferred to as ‘eddy rich’) using the hydrostatic configuration of the Massachusetts Insti-
 120 tute of Technology general circulation model (MITgcm; J. Marshall et al., 1997). We have
 121 46 vertical levels increasing from 6 m near the surface to 250 m at depth. Harmonic, bi-
 122 harmonic horizontal and vertical viscosity values of $A_{h2} = 20 \text{ m}^2 \text{ s}^{-1}$, $A_{h4} = -10^{10} \text{ m}^4 \text{ s}^{-1}$
 123 and $A_v = 10^{-5} \text{ m}^2 \text{ s}^{-1}$ were used respectively. For completeness, we provide a brief sum-
 124 mary of the configuration below.

125 Figure 1 shows the bathymetry of the modelled domain extending from 20°S to 55°N .
 126 In order to save computational time and memory allocation, the North Atlantic basin
 127 was configured to zonally wrap around periodically. Open boundary conditions are ap-
 128 plied at the north and south boundaries of our domain and Strait of Gibraltar, such that
 129 oceanic velocities (\mathbf{u}) and tracers (θ, s) are restored with a 36 minutes relaxation time
 130 scale toward a state derived by an ocean-only global Nucleus for European Modelling
 131 of the Ocean (NEMO) simulation (Molines et al., 2014, ORCA12.L46-MJM88 run in their
 132 paper, hereon referred to as ORCA12). The open boundary conditions are prescribed
 133 every five days from the ORCA12 run and linearly interpolated in between. A sponge
 134 layer is further applied to two adjacent grid points from the open boundaries where model
 135 variables are restored toward boundary conditions with a one-day relaxation time scale.
 136 In total, relaxation is applied along three grid points from the boundaries with it being
 137 the strongest at the boundary along with radiation conditions at the northern/southern
 138 most boundary. Although relatively short, no adverse effects were apparent upon inspec-
 139 tion in response to these relaxation time scales; e.g. changes in the open boundary con-
 140 ditions were seen to induce a physically consistent Atlantic Meridional Overturning Cir-
 141 culation response inside the domain (Jamet et al., 2020).

142 The 48-member ensemble was constructed as follows: 48 oceanic states separated
 143 by 24 hours each were taken during an initial month-long integration beginning Decem-
 144 ber 8, 1962. Simulations initialized with these states were run under yearly *repeating* 1963
 145 atmospheric and boundary conditions. At the surface, the ocean is partially coupled to
 146 an atmospheric boundary layer model (CheapAML; Deremble et al., 2013). In Cheap-
 147 AML, atmospheric surface temperature and relative humidity respond to ocean surface

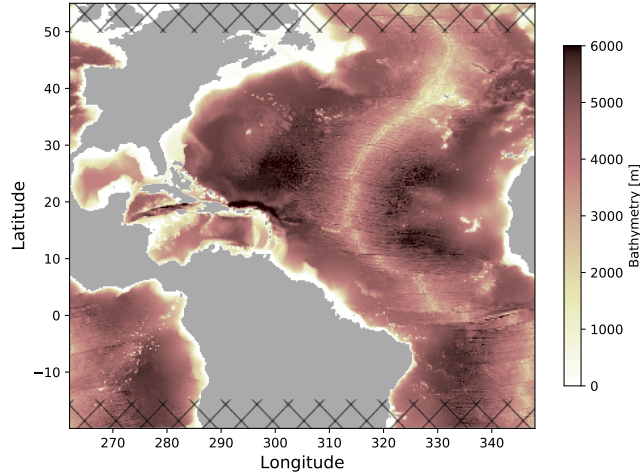


Figure 1. Bathymetry of the modelled domain. The domain was configured to wrap around zonally in order to save computation and memory allocation when generating the ensemble. The hatches indicate the northern and southern regions excluded from our analysis.

148 structures by exchanges of heat and humidity computed according to the Coupled Ocean–Atmosphere
 149 Response Experiment (COARE3; Fairall et al., 2003) flux formula, but are strongly re-
 150 stored toward prescribed values over land; there are no zonally propagating signals of
 151 climate teleconnection. The prescribed atmospheric state is taken from the Drakkar forc-
 152 ing set and boundary forcing from the ORCA12 run (details are given in Jamet et al.,
 153 2019a). After a year of integration from the 48 states, the last time step from each sim-
 154 ulation was taken as the initial condition for the ensuing ensemble members; each spun-
 155 up initial oceanic state is physically consistent with the atmospheric and boundary con-
 156 ditions of January 1, 1963 (details are given in Jamet et al., 2020). The ensemble mem-
 157 bers are then integrated forward in time for 5 years (1963–1967), and exposed to the same
 158 prescribed atmospheric state above the boundary layer and relaxation at the north/south
 159 boundaries across all ensemble members. (Note that the forcing and relaxation are no
 160 longer cyclic after the one-year spin-up phase.) During this interval, the oceanic state
 161 and the atmospheric boundary layer temperature and humidity evolve in time. In the
 162 following, we interpret the ensemble mean as the ocean response to the atmospheric state
 163 prescribed above the atmospheric boundary layer as well as the oceanic conditions im-
 164 posed at the open boundaries of the regional domain, while the ensemble spread is at-
 165 tributed to intrinsic ocean dynamics that develop at mesoscale-permitting resolution (Sérazin
 166 et al., 2017; Leroux et al., 2018; Jamet et al., 2019b).

167 The model outputs were saved as five-day averages. In the context of mesoscale dy-
 168 namics, which is the focus of this study, some temporal averaging is appropriate in or-
 169 der to filter out temporal scales shorter than the mesoscale eddies themselves. From a
 170 probabilistic perspective, the five-day averaging results in more Gaussian-like eddy statis-
 171 tics (based on the central-limit theorem). From a dynamical point of view, this does not
 172 allow us to close the residual-mean and eddy budgets (cf. G. Stanley, 2018, Section 4.4).
 173 Nevertheless, the ensemble dimension of our dataset provides an unique opportunity to
 174 examine the TWA eddy-mean flow interaction. In the following analysis, we exclude the
 175 northern and southern extent of 5° from our analysis to avoid effects from the open bound-
 176 ary conditions and sponge layer (Figure 1) and to maximize the signal of intrinsic vari-
 177 ability amongst the ensemble members. We also use the last year of output (1967) for
 178 the same reasons.

179 **3 Theory and implementation of thickness-weighted averaging**

180 The ocean is a stratified fluid, and the circulation and advection of tracers tend to
 181 align themselves along the stratified density surfaces. Hence, a natural way to under-
 182 stand the circulation is to consider the variables in a buoyancy framework and the residual-
 183 mean flow rather than the Eulerian mean flow. We leave the detailed derivation of the
 184 TWA framework to Young (2012, and references therein) and here, only provide a brief
 185 summary; the primitive equations in geopotential coordinates are first transformed to
 186 buoyancy coordinates upon which a thickness weighting and ensemble averaging along
 187 constant buoyancy surfaces are applied to obtain the TWA governing equations. Follow-
 188 ing the notation by Young (2012) and Ringler et al. (2017), the TWA horizontal momen-
 189 tum equations in the buoyancy coordinate system $(\tilde{t}, \tilde{x}, \tilde{y}, \tilde{b})$ are:

$$190 \quad \hat{u}_{\tilde{t}} + \hat{u}\hat{u}_{\tilde{x}} + \hat{v}\hat{u}_{\tilde{y}} + \hat{\omega}\hat{u}_{\tilde{b}} - f\hat{v} + \overline{m}_{\tilde{x}} = -\bar{\mathbf{e}}_1 \cdot (\tilde{\nabla} \cdot \mathbf{E}) + \hat{\mathcal{X}} \quad (1)$$

$$191 \quad \hat{v}_{\tilde{t}} + \hat{u}\hat{v}_{\tilde{x}} + \hat{v}\hat{v}_{\tilde{y}} + \hat{\omega}\hat{v}_{\tilde{b}} + f\hat{u} + \overline{m}_{\tilde{y}} = -\bar{\mathbf{e}}_2 \cdot (\tilde{\nabla} \cdot \mathbf{E}) + \hat{\mathcal{Y}} \quad (2)$$

193 where $\overline{(\cdot)}$ and $\widehat{(\cdot)} \stackrel{\text{def}}{=} \sigma^{-1} \overline{(\cdot)}$ are the ensemble averaged and TWA variables respectively
 194 where $\sigma (= \zeta_{\tilde{b}})$ is the thickness and ζ the depth of an iso-surface of buoyancy. The sub-
 195 scripts denote partial derivatives. The Montgomery potential is $m = \tilde{\phi} - \tilde{b}\zeta$ where $\tilde{\phi}$
 196 is the dynamically active part of hydrostatic pressure. ϖ is the dia-surface velocity across
 197 buoyancy contours, which we detail below for a realistic equation of state (EOS) for den-
 198 sity. The vectors $\bar{\mathbf{e}}_1 = \mathbf{i} + \bar{\zeta}_{\tilde{x}}\mathbf{k}$ and $\bar{\mathbf{e}}_2 = \mathbf{j} + \bar{\zeta}_{\tilde{y}}\mathbf{k}$ form the basis vectors spanning the
 199 buoyancy horizontal space where \mathbf{i} , \mathbf{j} and \mathbf{k} are the Cartesian geopotential unit vectors,

200 and \mathbf{E} is the E-P flux tensor described in detail in Section 4.1. Although each ensemble
 201 member has an individual basis $(\mathbf{e}_1, \mathbf{e}_2)$, the E-P flux divergence yields no cross terms
 202 upon averaging as the TWA operator commutes with the divergence of \mathbf{E} (for mathe-
 203 matical details, see Section 3.4 in Maddison & Marshall, 2013); this allows for the ten-
 204 sor expression in equations (1) and (2). \mathcal{X} and \mathcal{Y} are the viscous and forcing terms.

205 One subtle yet important point involves the buoyancy coordinate (\tilde{b}) for a realis-
 206 tic, non-linear EOS (Jackett & McDougall, 1995). The analysis in Young (2012) implic-
 207 itly assumes a linear EOS. With a realistic EOS, defining the vertical coordinate using
 208 potential density introduces errors. However, what constitutes a better buoyancy vari-
 209 able is the subject of some debate (e.g. Montgomery, 1937; Jackett & McDougall, 1997;
 210 McDougall & Jackett, 2005; de Szoeke & Springer, 2009; Klocker et al., 2009; Tailleux,
 211 2016; Lang et al., 2020). Although other choices are possible, we argue for the use of in-
 212 situ density *anomaly* ($\delta \stackrel{\text{def}}{=} \rho - \tilde{\rho}(z)$ where ρ is the in-situ density and $\tilde{\rho}$ is a function
 213 of only depth; Montgomery, 1937; G. J. Stanley, 2019). With density anomaly, buoyancy
 214 can be defined as:

$$215 \quad \tilde{b} \stackrel{\text{def}}{=} -\frac{g}{\rho_0} \delta \stackrel{\text{def}}{=} \tilde{b} \quad (3)$$

216 where \tilde{b} denotes the vertical coordinate and $\rho_0 = 999.8 \text{ kg m}^{-3}$ the Boussinesq refer-
 217 ence density prescribed in MITgcm. The undertilde is kept to remind the reader that
 218 buoyancy is defined with density anomaly. The question becomes how to choose $\tilde{\rho}(z)$
 219 so that monotonicity is maintained ($\tilde{b}_{\tilde{z}} > 0$). The vertical derivative of the in-situ den-
 220 sity anomaly can be decomposed as:

$$221 \quad \delta_z = \rho_z - \frac{d}{dz} \tilde{\rho} = \rho_\Phi \frac{d\Phi}{dz} - \frac{d}{dz} \tilde{\rho} = \frac{-\rho_0 g}{c_s^2} - \frac{d}{dz} \tilde{\rho}, \quad (4)$$

222 where $\Phi = -\rho_0 g z$ is the dynamically non-active part of hydrostatic pressure and c_s is
 223 the sound speed. For simplicity, we can write $\frac{d}{dz} \tilde{\rho} \stackrel{\text{def}}{=} -\rho_0 g \mathcal{C}_s^{-2}$ where $\mathcal{C}_s = \mathcal{C}_s(z)$ is a
 224 function of only depth, which yields:

$$225 \quad \tilde{b}_{\tilde{z}} = -\frac{g}{\rho_0} \delta_z = g^2 \frac{\mathcal{C}_s^2 - c_s^2}{c_s^2 \mathcal{C}_s^2}. \quad (5)$$

226 Denoting $\mathcal{C}_s = c_s + \Delta$ where $c_s^{-1} \Delta \ll 1$, the right-hand side (RHS) of equation (5)
 227 becomes:

$$228 \quad g^2 \frac{(c_s + \Delta)^2 - c_s^2}{c_s^2 \mathcal{C}_s^2} \approx \frac{g^2}{\mathcal{C}_s^2} \left[\left(1 + \frac{2\Delta}{c_s}\right) - 1 \right] = \frac{2g^2 \Delta}{c_s \mathcal{C}_s^2} \sim O(10^{-6}). \quad (6)$$

229 Hence, so long as $\mathcal{C}_s \gtrsim c_s$, monotonicity is assured while removing a large portion of
 230 compressibility, i.e. the iso-surfaces of \tilde{b} become close to neutral surfaces. In practice,

231 we chose \mathcal{C}_s to be larger than the maximum sound speed by 10^{-5} m s⁻¹ at each depth
 232 over the entire ensemble in order to avoid a singularity (viz. $\tilde{b}_{\sim z} = 0$). With \mathcal{C}_s deter-
 233 mined, integrating for $\tilde{\rho}$ gives:

$$234 \quad \tilde{\rho} = - \int_z^0 \frac{\rho_0 g}{\mathcal{C}_s} dz + \rho_0, \quad (7)$$

235 which reduces to $\tilde{\rho}|_{z=0} = \rho_0$. The buoyancy equation using the in-situ density anomaly
 236 becomes:

$$237 \quad \frac{D}{Dt} \tilde{b} = \tilde{b}_{\sim \theta} \dot{\theta} + \tilde{b}_{\sim s} \dot{s} + \tilde{b}_{\sim z} \frac{Dz}{Dt} \quad (8)$$

$$238 \quad = \mathcal{B} + wg^2 \frac{\mathcal{C}_s^2 - c_s^2}{c_s^2 \mathcal{C}_s^2}, \quad (9)$$

239 where $\mathcal{B} \stackrel{\text{def}}{=} \tilde{b}_{\sim \theta} \dot{\theta} + \tilde{b}_{\sim s} \dot{s}$, and $\dot{\theta}$ and \dot{s} are the net diabatic contributions on potential tem-
 240 perature and practical salinity respectively, which we approximate by diagnosing off-line
 241 the sum of harmonic and biharmonic diffusion below the mixed layer using the five-day
 242 averaged outputs of θ and s . We summarize the RHS of (9) as the dia-surface velocity
 243 $\varpi \stackrel{\text{def}}{=} \mathcal{B} + wg^2 \frac{\mathcal{C}_s^2 - c_s^2}{c_s^2 \mathcal{C}_s^2}$.

244 A further requirement of the TWA framework is that the pressure anomaly defined
 245 by such buoyancy coordinate translates into a body force in the buoyancy coordinate
 246

$$247 \quad \nabla_{\tilde{h}} \phi(z) \mapsto \nabla_{\tilde{h}} \phi(\tilde{b}) = \tilde{\nabla}_{\tilde{h}} m, \quad (10)$$

248 where the subscript $(\cdot)_{\tilde{h}}$ represents the horizontal gradient and $\tilde{\nabla}_{\tilde{h}} = (\partial_{\tilde{x}}, \partial_{\tilde{y}})$. Using
 249 in-situ buoyancy anomaly, the pressure anomaly becomes:

$$250 \quad \phi(z) = \int \tilde{b} dz, \quad (11)$$

251 while the pressure anomaly for a Boussinesq hydrostatic fluid is:

$$252 \quad \phi(z) = \int -\frac{g}{\rho_0} (\rho - \rho_0) dz. \quad (12)$$

253 Since $\tilde{\rho}$ is only a function of depth, the horizontal gradient of the two remain identical
 254 ($\nabla_{\tilde{h}} \tilde{\phi} = \nabla_{\tilde{h}} \phi$) and equation (10) holds. (We note that equation (10) does not hold for
 255 pressure anomaly defined by potential density when the EOS is non-linear, and while
 256 more elaborate techniques may improve the neutrality of δ , the relation to the dynam-
 257 ics is non-trivial for other density variables such as neutral and orthobaric densities.) The
 258 use of in-situ density anomaly to define the buoyancy coordinate maintains the desir-
 259 able properties of a unique, statically stable vertical coordinate and a simple hydrostatic

260 balance ($\sigma = \zeta_{\tilde{b}} = -m_{\tilde{b}\tilde{b}}$) while removing roughly 99% of the effect of compressibility
 261 basin wide at each depth ($\frac{g^2(c_s^{-2}-C_s^{-2})}{g^2c_s^{-2}} \approx \frac{2c_s\Delta}{C_s^2} \sim O(10^{-2})$). For a non-linear EOS, a
 262 material conservation of potential vorticity (PV) and non-acceleration conditions do not
 263 exist (cf. Vallis, 2017, Chapter 4). Discussion regarding the energetics are given in Ap-
 264 pendix A.

265 The raw simulation outputs were in geopotential coordinates so we first remapped
 266 all of the variables in equations (1) and (2) onto 55 buoyancy levels spread across the
 267 range of $\tilde{b} \in (-0.196, -0.287) \text{ m s}^{-2}$ (with the mathematical formulation of $\delta = \delta_0 +$
 268 $A_\delta \frac{\tanh(\tau) - \tanh(0)}{\tanh(\tau_{\max}) - \tanh(0)}$ where $\delta_0 = 20 \text{ kg m}^{-3}$, $A_\delta = 9.2 \text{ kg m}^{-3}$, and $\tau \in [0, 2)$ in order
 269 to account for the abyssal weak stratification):

$$270 \quad (u, v, \tilde{b}, \nabla_{\tilde{h}}\phi, \theta, s, \varpi)(t, x, y, z) \mapsto (u, v, \zeta, \tilde{\nabla}_{\tilde{h}}m, \theta, s, \varpi)(\tilde{t}, \tilde{x}, \tilde{y}, \tilde{b}) \quad (13)$$

271 using the `fastjmd95` Python package to compute the in-situ density and its partial deriva-
 272 tives (Abernathey, 2020), and the `xgcm` Python package (Abernathey et al., 2021; Jones
 273 et al., 2020; Busecke & Abernathey, 2020) which allows for coordinate remapping con-
 274 sistent with the finite-volume discretization of MITgcm. The horizontal velocity vector
 275 becomes $u\mathbf{i} + v\mathbf{j} \mapsto u\mathbf{e}_1 + v\mathbf{e}_2$. For the horizontal pressure anomaly gradient, we re-
 276 computed the pressure anomaly using the five-day averaged outputs have and have in-
 277 voked the identity (10).

278 4 Results

279 We start by showing the time series of domain-averaged horizontal kinetic energy
 280 (KE) and potential temperature, and an arbitrary buoyancy iso-surface (Figure 2). Fig-
 281 ure 2a shows the simulation has a prominent seasonal cycle with the KE and temper-
 282 ature both peaking in summer. In Figure 2, we also show the residual-mean fields on Jan-
 283 uary 3, 1967, the first day of the year of output we analyze. The depth of the buoyancy
 284 level shown in Figure 2c is below the ensemble-mean mixed-layer depth (MLD; Figure 2b)
 285 basin wide where diabatic effects are small, but is shallow enough to capture the imprint
 286 of the Gulf Stream; the iso-surface shoals drastically across the latitude of $\sim 38^\circ\text{N}$ where
 287 the separated Gulf Stream is situated (Figure 2d). The ensemble-mean MLD was com-
 288 puted as the depth at which the potential density computed from ensemble-mean tem-
 289 perature and salinity fields increased by 0.03 kg m^{-3} from the density at 10 m depth ($\overline{\text{MLD}} \stackrel{\text{def}}{=} \text{MLD}(\bar{\theta}, \bar{s})$; de Boyer Montégut et al., 2004). The residual-mean KE field ($\text{MKE}, K^\# \stackrel{\text{def}}{=} |\hat{\mathbf{u}}|^2/2$;
 290 Figure 2d) shows the characteristic features of the Gulf Stream, North Brazil Cur-
 291

292 rent and equatorial undercurrent. The North Brazil Current, although having large val-
 293 ues in \overline{KE} , shows no imprint on the buoyancy depth (Figure 2c). The residual-mean Rossby
 294 number ($Ro^\# \stackrel{\text{def}}{=} f^{-1}(\hat{v}_x - \hat{u}_y)$) shown in Figure 2e is smaller than unity indicating that
 295 over most of the North Atlantic basin, the residual-mean flow in the interior is balanced
 296 in our model with the exception of regions with energetic currents, e.g. the Gulf Stream,
 297 loop current in the Gulf of Mexico and the North Brazil Current. Near the equator, the
 298 Coriolis parameter becomes small leading to large Rossby numbers. The kinematics of
 299 discretizing the gradients in buoyancy coordinates are given in Appendix B. We now move
 300 on to examine the eddy feedback onto the (residual) mean flow. Hereon, we drop the pre-
 301 fix ‘residual’ unless required for clarity.

302 4.1 The Eliassen-Palm flux

303 The E-P flux tensor (\mathbf{E}) in the TWA framework (eqns. (1) and (2)) is:

$$304 \mathbf{E} = \begin{pmatrix} \widehat{u''u''} + \frac{1}{2\bar{\sigma}}\overline{\zeta'^2} & \widehat{u''v''} & 0 \\ \widehat{v''u''} & \widehat{v''v''} + \frac{1}{2\bar{\sigma}}\overline{\zeta'^2} & 0 \\ \overline{\varpi''u''} + \frac{1}{\bar{\sigma}}\overline{\zeta'm'_x} & \overline{\varpi''v''} + \frac{1}{\bar{\sigma}}\overline{\zeta'm'_y} & 0 \end{pmatrix} \quad (14)$$

305 where $(\cdot)'' = (\cdot) - \widehat{(\cdot)}$ and $(\cdot)' = (\cdot) - \overline{(\cdot)}$ are the residual from the thickness-weighted
 306 and ensemble averages respectively (Maddison & Marshall, 2013; Aoki, 2014; Ringler et
 307 al., 2017). The two are related via the (eddy-induced) bolus velocity (Greatbatch, 1998;
 308 McDougall & McIntosh, 2001):

$$309 \mathbf{u}'' = \mathbf{u} - \frac{\bar{\sigma}\mathbf{u}}{\bar{\sigma}} = \bar{\mathbf{u}} + \mathbf{u}' - \frac{(\bar{\sigma} + \sigma')(\bar{\mathbf{u}} + \mathbf{u}')}{\bar{\sigma}} \quad (15)$$

$$310 = \mathbf{u}' + \frac{\sigma'\mathbf{u}'}{\bar{\sigma}}. \quad (16)$$

311

312 We show each term in equation (14) in Figure 3. The Reynolds stress term $\widehat{u''v''}$ is as-
 313 sociated with barotropic processes in analogy to atmospheric jets (Figure 3a; Aoki et al.,
 314 2016; Jamet et al., 2021; Vallis, 2017, Chapter 15). The eddy momentum flux terms $(\widehat{u''^2}, \widehat{v''^2})$
 315 in Figure 3c,d are seen to exchange momentum between eddies and the mean flow, i.e.
 316 to accelerate or decelerate the Gulf Stream as they affect the horizontal shear upon tak-
 317 ing their gradients. The term due to the vertical displacement of buoyancy layer $(\frac{1}{2\bar{\sigma}}\overline{\zeta'^2})$
 318 is related to the eddy potential energy (EPE; cf. equations A27-A30). The interfacial
 319 form stress $\overline{(\zeta'\tilde{\nabla}_h m')}$; Figure 3e,f) associated with baroclinic instability is “deceiv-
 320 ingly” orders of magnitude smaller than the other terms. However, it is the divergence of the
 321 E-P flux and not the flux itself that goes into the momentum equations, and the hor-

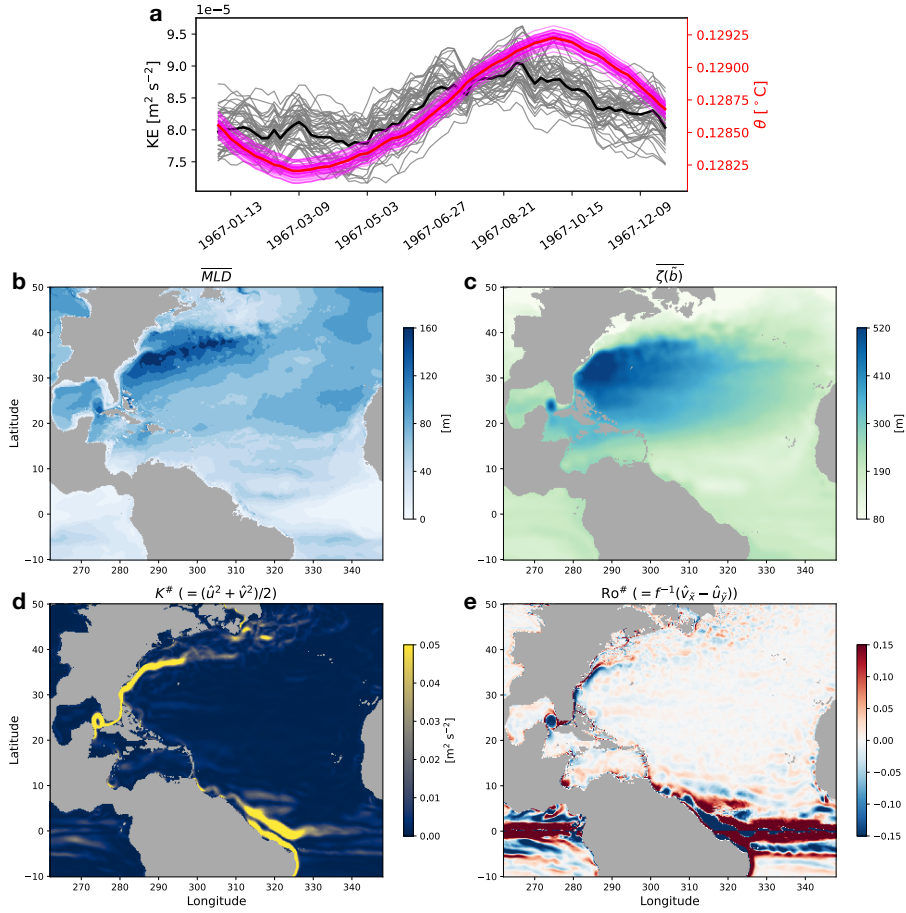


Figure 2. Time series of the domain-averaged total KE (black) and potential temperature (red) for the 48 ensemble members between 15°S - 50°N . The thick lines show the ensemble mean and the thin lines each ensemble member **a**. **b,c** The ensemble-mean MLD on January 3, 1967 and depth of the iso-surface of buoyancy $\bar{b} = -0.26 \text{ m s}^{-2}$. **d,e** The residual-mean KE ($K^{\#}$) and Rossby number ($\text{Ro}^{\#}$) on the same buoyancy surface.

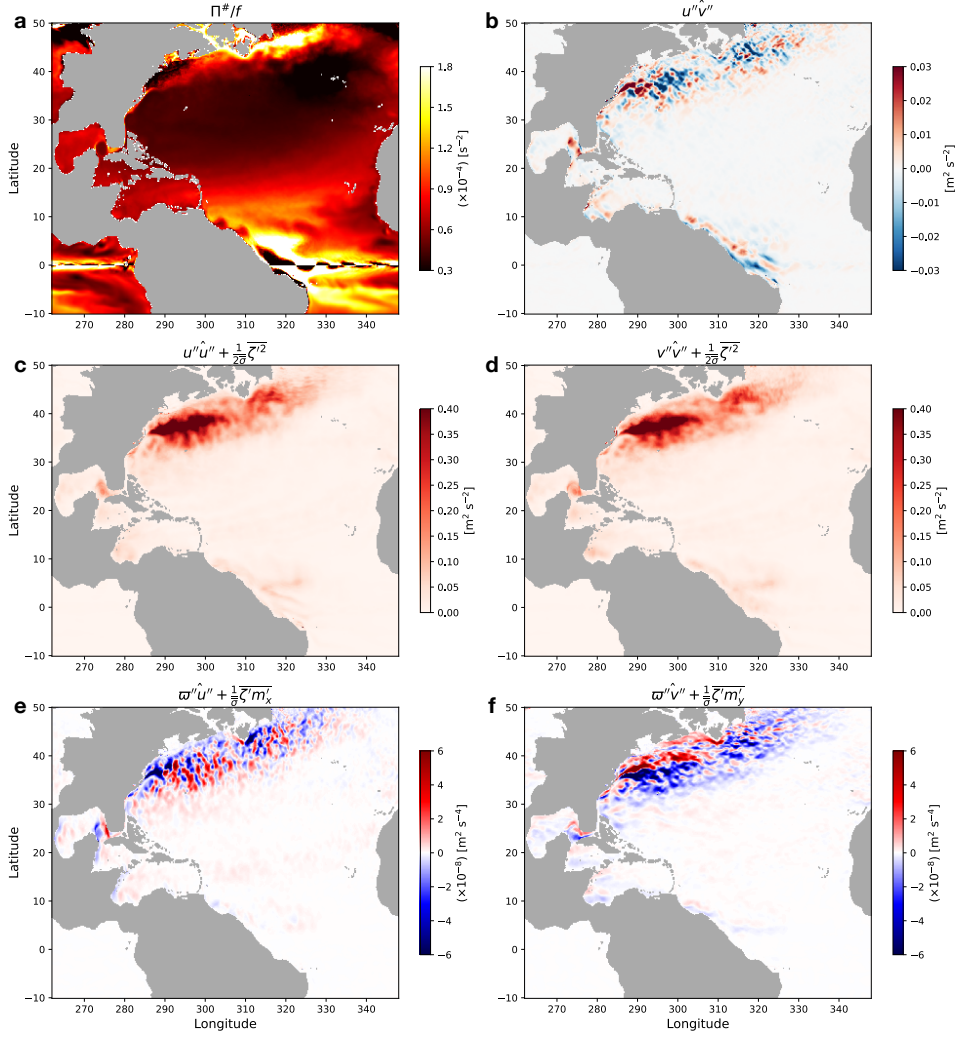


Figure 3. The residual-mean Ertel potential vorticity normalized by the local Coriolis parameter ($\Pi^\# / f \stackrel{\text{def}}{=} \bar{\sigma}^{-1}(1 + \text{Ro}^\#)$) **a** and terms in the E-P flux tensor **b-f** on January 3, 1967 on the iso-surface of buoyancy as in Figure 2. Note the scaling factors on panels a, e and f.

322 horizontal ($\tilde{\nabla}_h$) and vertical gradient ($\partial_{\tilde{z}}$) differ by roughly $O(10^6)$. The contribution from
 323 the adiabatic and compressibility effects (i.e. the terms with ϖ) were smaller than the
 324 interfacial form stress by another order of magnitude or more in the subtropics (not shown).
 325 It is quite surprising that the signals in the equatorial undercurrent region, although hav-
 326 ing relatively high KE (Figure 2d), are significantly smaller than in the Gulf Stream and
 327 North Brazil Current regions, virtually not visible in Figure 3. This implies that the mean
 328 flow dominates over the eddies in the equatorial region.

329 Writing out the E-P flux divergence in eqns. (1) and (2) gives:

330
$$-\bar{\mathbf{e}}_1 \cdot (\tilde{\nabla} \cdot \mathbf{E}) = -\bar{\sigma}^{-1} \left([\overline{\sigma(u''u'')} + \frac{1}{2\bar{\sigma}} \overline{\zeta'^2}]_{\bar{x}} + [\overline{\sigma v''u''}]_{\bar{y}} + [\overline{\sigma(\varpi''u''} + \frac{1}{\bar{\sigma}} \overline{\zeta' m'_{\bar{x}}})]_{\bar{b}} \right) \quad (17)$$

331
$$= -\bar{\sigma}^{-1} \left([\overline{\sigma u''u''} + \overline{\zeta'^2}/2]_{\bar{x}} + [\overline{\sigma v''u''}]_{\bar{y}} + [\overline{\sigma \varpi''u''} + \overline{\zeta' m'_{\bar{x}}}]_{\bar{b}} \right), \quad (18)$$

332
$$\stackrel{\text{def}}{=} -(E_{\bar{x}}^{00} + E_{\bar{y}}^{10} + E_{\bar{b}}^{20}) \quad (19)$$

333

334

335
$$-\bar{\mathbf{e}}_2 \cdot (\tilde{\nabla} \cdot \mathbf{E}) = -\bar{\sigma}^{-1} \left([\overline{\sigma u''v''}]_{\bar{x}} + [\overline{\sigma(v''v''} + \frac{1}{2\bar{\sigma}} \overline{\zeta'^2})]_{\bar{y}} + [\overline{\sigma(\varpi''v''} + \frac{1}{\bar{\sigma}} \overline{\zeta' m'_{\bar{y}}})]_{\bar{b}} \right) \quad (20)$$

336
$$= -\bar{\sigma}^{-1} \left([\overline{\sigma u''v''}]_{\bar{x}} + [\overline{\sigma v''v''} + \overline{\zeta'^2}/2]_{\bar{y}} + [\overline{\sigma \varpi''v''} + \overline{\zeta' m'_{\bar{y}}}]_{\bar{b}} \right), \quad (21)$$

337
$$\stackrel{\text{def}}{=} -(E_{\bar{x}}^{01} + E_{\bar{y}}^{11} + E_{\bar{b}}^{21}). \quad (22)$$

338

339 As the signal in the North Atlantic basin is the largest in the separated Gulf Stream re-
 340 gion (Figure 3), we show each term in the E-P flux divergence north of 25°N (Figure 4).
 341 The large signal is consistent with Jamet et al. (2021) where they found the subtropi-
 342 cal gyre to be a Fofonoff-like inertial circulation (Fofonoff, 1981), and that the separated
 343 jet was where the energy input from surface winds were predominantly lost to eddies.
 344 The divergence of interfacial form stress ($E_{\bar{b}}^{20}, E_{\bar{b}}^{21}$) becomes larger than the divergence
 345 of the Reynolds stress terms ($E_{\bar{y}}^{10}, E_{\bar{x}}^{01}$), which are the smallest amongst the three terms
 346 in the E-P flux convergence (Figure 4b,c). The contribution from the terms with dia-
 347 surface velocity (ϖ'') was roughly two-orders of magnitude smaller than the other terms
 348 in the E-P flux convergence in the adiabatic interior (not shown), which supports the
 349 neutrality of δ to define the buoyancy surfaces. Right at the separation of the Gulf Stream
 350 west of 290°E and around 36°N, the convergence of eddy momentum flux and potential
 351 energy, and interfacial form stress (i.e. baroclinic instability) tend to counteract each other;
 352 in the zonal direction, the eddy momentum flux and potential energy convergence tends
 353 to decelerate the Gulf Stream while as baroclinic instability tends to accelerate it (Fig-
 354 ure 4a,e). The repeating positive and negative features further downstream are roughly
 355 on the scales of the Rossby deformation radius, consistent with Uchida, Deremble, De-
 356 war, and Penduff (2021) where they diagnosed the E-P flux convergence from a 101-member
 357 quasi-geostrophic double-gyre ensemble. In the meridional direction, the eddy momen-
 358 tum flux and potential energy convergence tends to smooth out the Gulf Stream (decel-
 359 erate the jet in the subpolar gyre by injecting northward momentum, and southward mo-
 360 mentum in the subtropical gyre) while baroclinic instability tends to sharpen it (Figure 4d,f).

361

362 We now examine further details in the separated Gulf Stream, a region where ed-
 363 dies have been shown to modulate the mean flow structure (e.g. Cronin, 1996; Chassignet

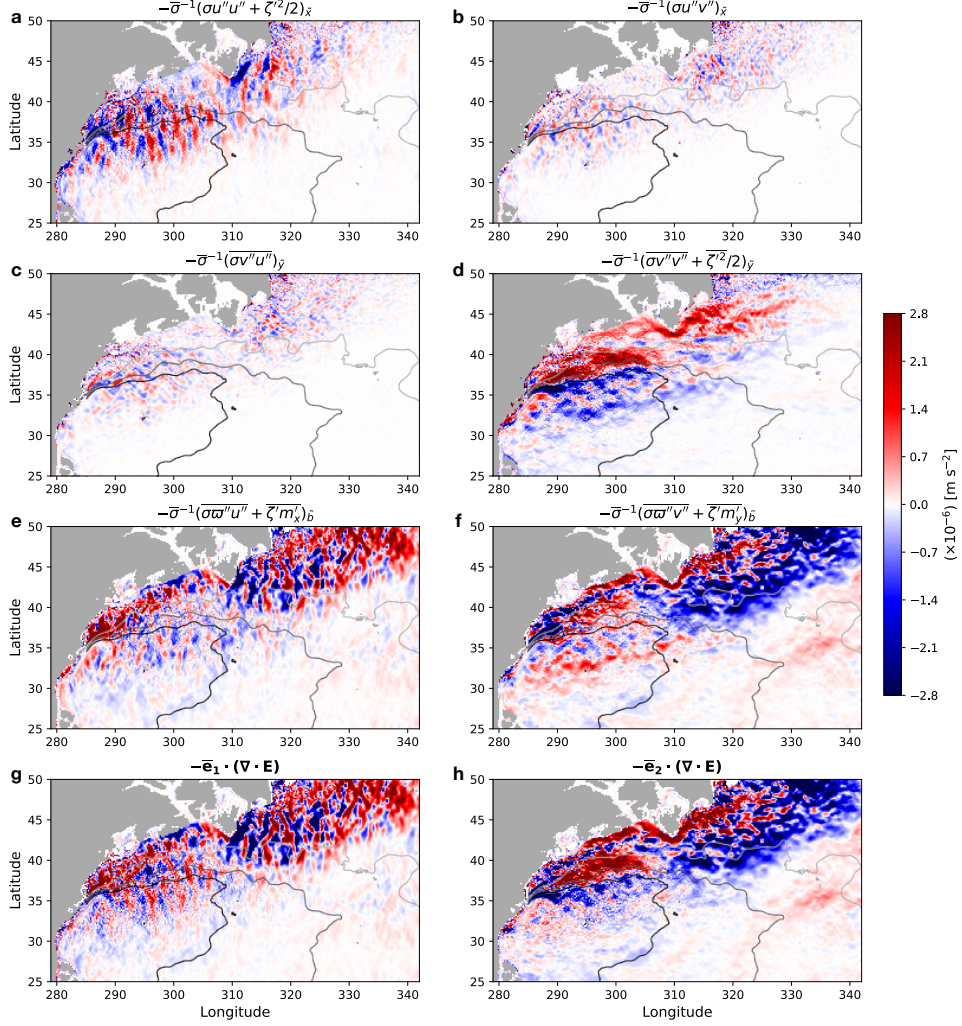


Figure 4. The terms in the convergence of E-P flux tensor on January 3, 1967 on the iso-surface of $\tilde{b} = -0.26 \text{ m s}^{-2}$ **a-f**. Positive values (red shadings) indicate the eddies fluxing momentum to the mean flow and vice versa. The panels are laid out so that summing up the top three rows per column yields the total zonal ($-\bar{\mathbf{e}}_1 \cdot (\tilde{\nabla} \cdot \mathbf{E})$) **g** and meridional E-P flux divergence ($-\bar{\mathbf{e}}_2 \cdot (\tilde{\nabla} \cdot \mathbf{E})$) **h** respectively. The contours in grey shading east of 285°E indicate the 400, 300 and 200 m depth of the buoyancy surface.

364 & Xu, 2021), as seasonal means in order to capture representative features. Winter is
 365 defined as the months of January, February, March, and summer as July, August, Septem-
 366 ber. Upon separation, the zonal E-P flux convergence tends to decelerate the Gulf Stream.
 367 The repeating features of positive and negative values for the zonal component of the
 368 E-P flux convergence persist and are likely associated to the jet meandering (Figure 5a,c).
 369 In the meridional direction, the E-P flux convergence tends to smooth out the separated
 370 Gulf Stream in the meridional direction (decelerate the jet northwards in the subtrop-
 371 ical gyre on the North flank of the separated Gulf Stream and southwards in the sub-
 372 polar gyre; Figure 4b,d) although this largely being contained west of 310°E. East of 310°E,
 373 the E-P flux convergence tends to shift the North Atlantic Current east and southwards
 374 in the open ocean, while northwards closer to the continental rise. Examining the merid-
 375 ional transect averaged over the zonal extent of 290°E-305°E where the separated Gulf
 376 Stream is roughly zonal (Figure 2d), the separated Gulf Stream can be identified with
 377 the steep shoaling of the iso-surfaces of buoyancy between 36°N-40°N (Figure 5e-h). The
 378 overall magnitude and reversal in sign at the core of the jet (around 37.5°N) with dimin-
 379 ishing amplitude with depth for the zonal E-P flux divergence during winter ($-\bar{\mathbf{e}}_1 \cdot (\tilde{\nabla} \cdot$
 380 $\mathbf{E})$; Figures 5g, 6a,b) is roughly in agreement with Ringler et al. (2017, their Figure 6
 381 where the sign convention in equation (17) is reversed from ours for the eddy forcing term
 382 and their units are in [$\text{m s}^{-1} \text{ day}^{-1}$]) where they diagnosed an idealized zonally re-entrant
 383 jet. It is interesting to note, however, that the vertical structure of the E-P flux conver-
 384 gence is much smoother and barotropic during the summer with a consistent decelera-
 385 tion of the jet on its northern flank and acceleration on its southern flank (Figures 5g,
 386 6e,f).

387 In Figure 6, we show the vertical profile of the seasonal E-P flux convergence along
 388 with each component in equations (17) and (20) area averaged over the zonal extent of
 389 290°E-305°E. The E-P flux convergence closely follows that of the interfacial form stress
 390 convergence (i.e. baroclinic instability) with the Reynolds stress due to cross correlation
 391 between the zonal and meridional eddy momentum (E_y^{10}, E_x^{01} ; orange lines) taking the
 392 smallest magnitude. The amplitude of interfacial form stress convergence is larger near
 393 the surface (viz. larger buoyancy values), which is expected from the seasonal surface
 394 forcing affecting the isopycnal tilt and hence baroclinicity of the surface flow. The merid-
 395 ional smoothing of the separated Gulf Stream is also apparent from the vertical profiles
 396 with the meridional E-P flux convergence taking negative values on the southern flank

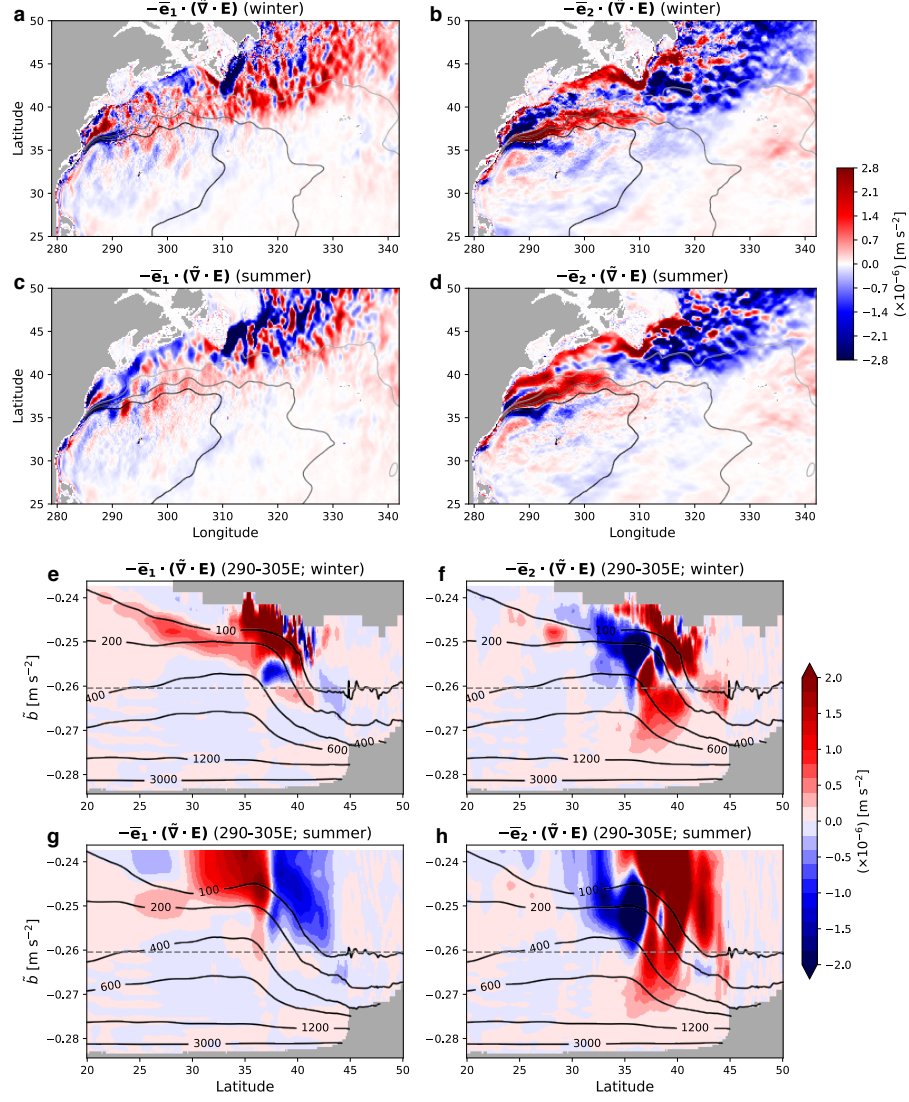


Figure 5. The seasonal mean of the zonal and meridional E-P flux convergence for winter and summer **a-d**. The contours in grey shading indicate the 400, 300 and 200 m depth of the buoyancy surface. **e-h** The zonal-mean transect between 290°E-305°E of the E-P flux convergence is shown in colored shading and ensemble-mean depth in black contours. The iso-surface of buoyancy used through Figures 2-4 is shown as the grey dashed line. The masked out region north of 30°N near the surface during winter is where the iso-surfaces of buoyancy outcrop across all ensemble members. We see that more buoyancy surfaces outcrop during winter.

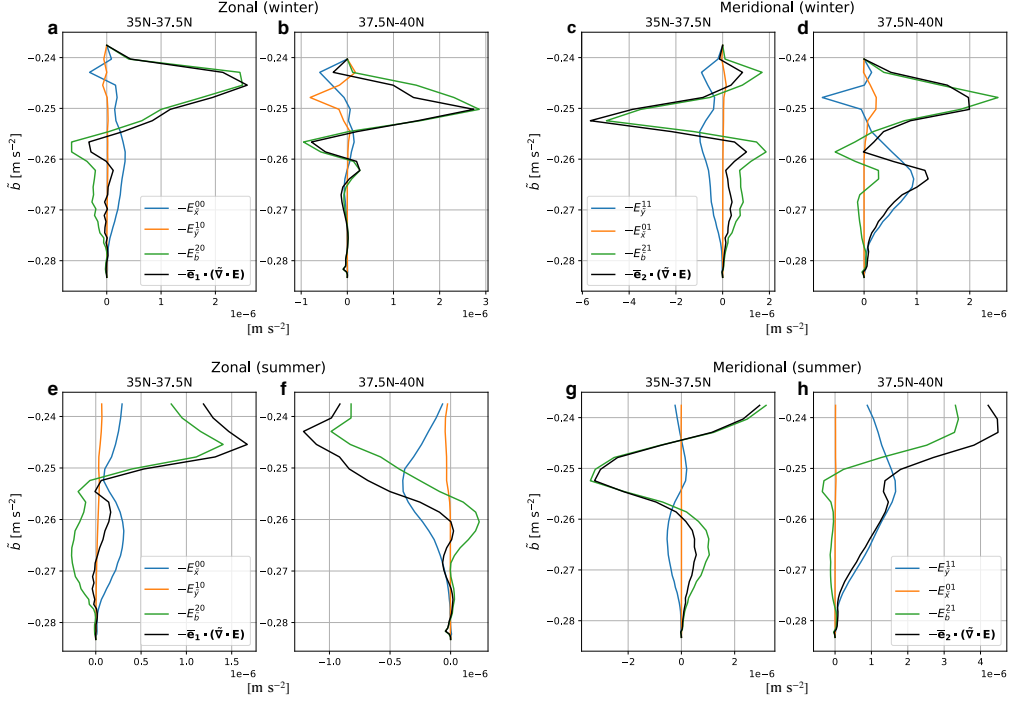


Figure 6. Vertical profile of the area-averaged, seasonal zonal and meridional E-P flux convergence north and south of the separated Gulf Stream over the zonal extent 290°E - 305°E . The area averaging is separated between 35°N - 37.5°N and 37.5°N - 40°N . The top panels show the seasonal mean for winter and bottom for summer.

397 of the jet and positive values on the northern flank. The convergence of eddy momen-
 398 tum flux and potential energy tends to mirror that of interfacial form stress (blue and
 399 green lines in Figure 6). This counteracting balance is consistent with what Aoki et al.
 400 (2016, the terms $\partial_x R^x$ and $\partial_z(R^z + F_a^+)$ in their Figures 5a and 6) found in the Kuroshio
 401 extension region.

4.2 The ergodic assumption

403 In this section, we replace the averaging operator with the temporal mean of the
 404 50 years of output ($\overline{(\cdot)}^t, (\cdot)^{t \text{ def}} (\cdot) - \overline{(\cdot)}^t$) from a single arbitrary realization (realiza-
 405 tion 00 to be specific) to examine the ergodic assumption and compare with our TWA
 406 results. Realization 00 was taken from a 24-member ensemble originally designed for a
 407 different study (Jamet et al., 2019b). The 48 members discussed above were constructed
 408 by adding 24 members to the first five years of this dataset. The TWA operator now be-
 409 comes $\widehat{(\cdot)}^t \text{ def } \overline{\sigma}^{t-1} \overline{\sigma(\cdot)}^t$ and eddies $(\cdot)^{t \text{ def}} (\cdot) - \widehat{(\cdot)}^t$. The maximum sound speed per

410 depth (C_s) was recomputed for the 50 years of realization 00 in remapping the coordi-
 411 nate system. Although the averaging operator is now along the time dimension, we note
 412 that this is different from the Temporal-Residual Mean (TRM) framework developed by
 413 McDougall and McIntosh (2001) in the sense that our variables are thickness weighted.
 414 The hope of applying the ergodic assumption to a temporally varying system, as we have
 415 shown in previous sections, is that for a sufficiently long time series, such sub- and inter-
 416 annual variability will cancel out with only the stationary feature being extracted in the
 417 ‘mean’ flow.

418 In Figure 7, we show the climatological E-P flux convergence from realization 00.
 419 In other words, all time scales shorter than 50 years are now relegated to the eddies. While
 420 having similar spatial structures to Figures 4 and 5a-d, they are more spread out with
 421 less detail. In particular, the seasonality is obscured by the climatological mean of 50
 422 years and becomes similar to the summertime of the 48-member ensemble (Figure 5c,d).
 423 In other words, it misses the variability we see during wintertime (Figure 5a,b). Con-
 424 sidering the 50-year time scale of averaging, the signals that emerge in the climatolog-
 425 ical E-P flux convergence are likely due to standing eddies. The climatological zonal-mean
 426 transect also resemble the ensemble summertime albeit with weaker amplitude (Figures 5e-
 427 h and 8) where the eddies tend to zonally decelerate the separated Gulf Stream on its
 428 northern flank and accelerate it on its southern flank (Figure 8a). In the meridional di-
 429 rection, the eddies tend to decelerate the subpolar gyre on the northern flank of the sep-
 430 arated Gulf Stream and the subtropical gyre on its southern flank (Figure 8b).

431 Taking the climatological time mean of 50 years of output is perhaps the most con-
 432 servative definition of the mean flow under ergodicity. We, therefore, now loosen the tem-
 433 poral averaging to a climatological annual cycle in defining the residual mean flow. In
 434 doing so, we chunk the 50 years into 50 annual segments and take their average to pro-
 435 duce a single segment of ~ 365 days. Namely, we treat each year as an individual re-
 436 alization of the ocean, generating a pseudo 50-member year-long ensemble. The eddies
 437 are now defined as fluctuations about this climatological annual cycle. In Figure 9, we
 438 show the MKE on a buoyancy level on January 3 with similar depths diagnosed from
 439 the ensemble and realization 00. While the maximum MKE amplitudes are similar, the
 440 mean flow is more spread out in realization 00. This likely comes from the different paths
 441 the Gulf Stream takes resulting as a response to different yearly atmospheric states, which
 442 get averaged all together. In other words, while the degrees of freedom are similar be-

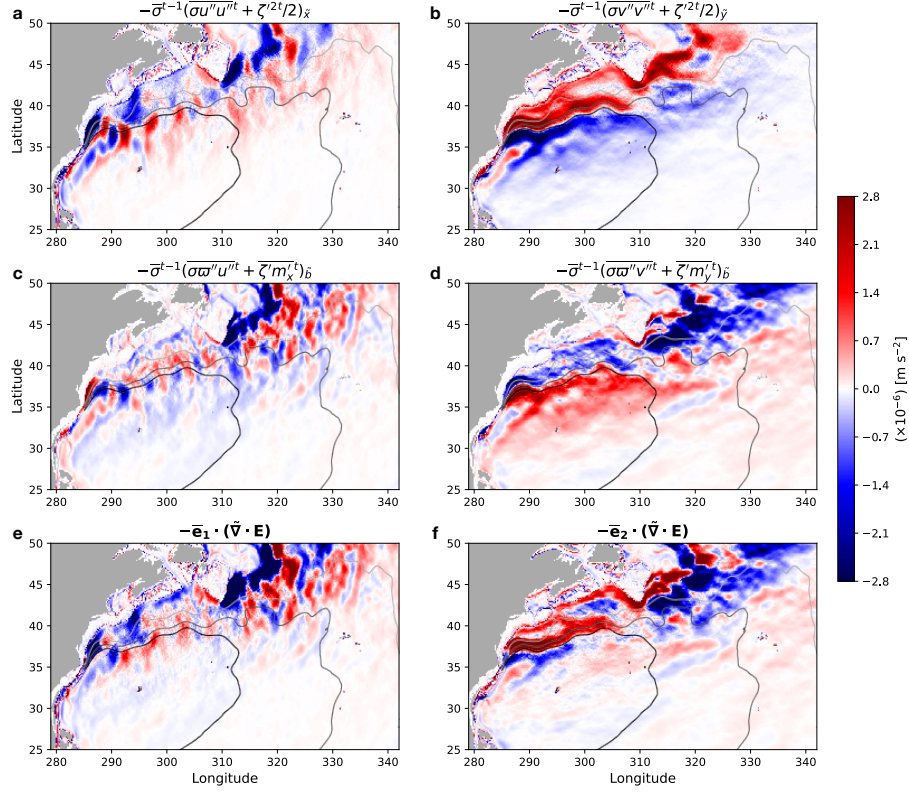


Figure 7. The terms in the climatological convergence of E-P flux tensor on the iso-surface of $\tilde{b} = -0.26 \text{ m s}^{-2}$ from realization 00 **a-d**. We do not show the terms due to the Reynolds stress ($\widehat{u''^t v''^t}$) as they were negligible compared to the other terms, and omit the superscript t on variables with primes to avoid the clutter. **e,f** Climatology of the total zonal ($-\bar{\mathbf{e}}_1 \cdot (\tilde{\nabla} \cdot \mathbf{E})$) and meridional E-P flux divergence ($-\bar{\mathbf{e}}_2 \cdot (\tilde{\nabla} \cdot \mathbf{E})$) respectively. The contours in grey shading east of 285°E indicate the 400, 300 and 200 m depth of the buoyancy surface.

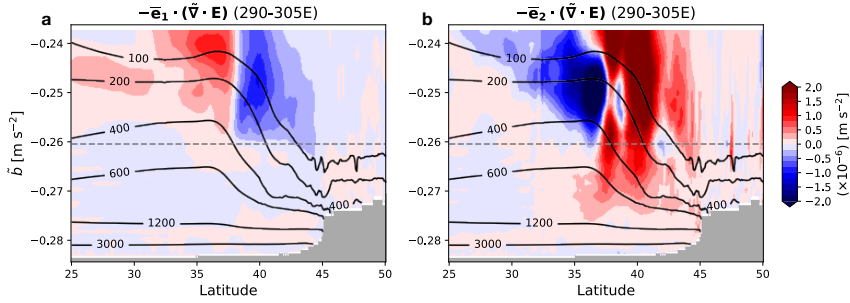


Figure 8. The climatological zonal-mean transect between 290°E - 305°E of the E-P flux convergence is shown in colored shading and ensemble-mean depth in black contours from realization 00 **a,b**. The iso-surface of buoyancy used in Figure 7 is shown as the grey dashed line.

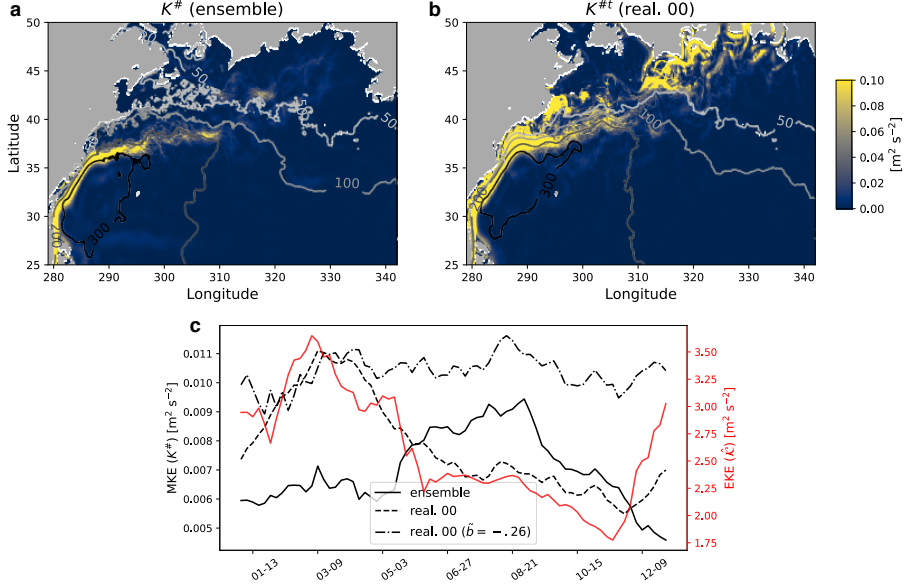


Figure 9. The (residual) mean KE on January 3 from the ensemble ($K^\#$) and realization 00 ($K^{\#t}$) on buoyancy levels with similar depth **a,b**. The regions with outcropping buoyancy surface are masked out. The colors indicate the MKE and contours in grey scaling show the depths for 50, 100, 200 and 300 m. **c** Time series of domain averaged MKE ($K^\#$ and $K^{\#t}$) in black plotted against the left y axis and EKE ($\widehat{\mathcal{K}}$) in red plotted against the right y axis. The domain was taken over the horizontal extent shown in panels a,b. Note the difference in magnitudes of order on the y axes.

443 between the ensemble (48 members) and realization 00 (50 members assuming a decorre-
 444 lation time scale of a year), the ensemble mean captures the oceanic response to the at-
 445 mospheric state specific to 1967. Realization 00, on the other hand, implies that 50 years
 446 are not sufficient for the ‘eddies’ to cancel out upon averaging for a climatological an-
 447 nual cycle and the mean flow becomes ill defined.

448 The imprint of fluctuations from each year onto the MKE domain averaged over
 449 the depths of $\sim 50\text{-}500$ m ($\tilde{b} \in (-0.25, -0.26)$) result in its seasonality to differ from the
 450 ensemble mean; realization 00 takes its maximum around March while the ensemble around
 451 August (black solid and dashed lines in Figure 9c respectively). However, the season-
 452 ality in the area averaged MKE from realization 00 on $\tilde{b} = -0.26$ shows a summertime
 453 maximum (black dot-dashed line in Figure 9c). This implies that the discrepancy be-
 454 tween $K^\#$ and $K^{\#t}$ results from the surface ocean being sensitive to the atmospheric
 455 state while being less so in the interior. Indeed, the domain averaged eddy KE (EKE;

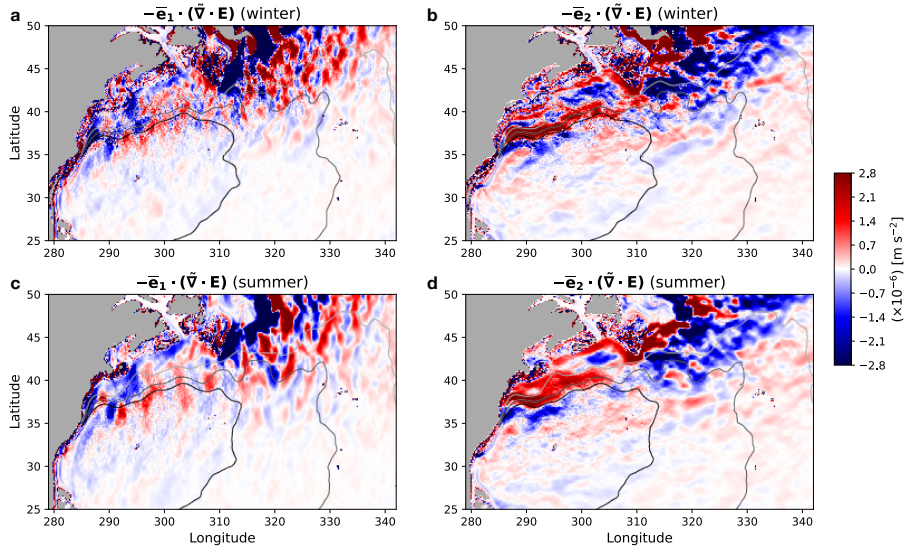


Figure 10. The E-P flux convergence from realization 00 for the climatological winter and summer on the iso-surface of $\tilde{b} = -0.26 \text{ m s}^{-2}$. The contours in grey shading east of 285°E indicate the 400, 300 and 200 m depth of the buoyancy surface.

see Appendix A for definition) diagnosed from the ensemble shows a maximum during
 456 winter when the surface ocean is more susceptible to baroclinic instability due to atmo-
 457 spheric cooling (red line in Figure 9c; Uchida et al., 2017). We conclude that in the pro-
 458 cess of creating a climatological annual cycle, we convolute the oceanic response to dif-
 459 ferent atmospheric states (i.e. interannual variability) and contaminate the eddy-mean
 460 flow decomposition. The ill defined mean flow also imprints itself onto the E-P flux con-
 461 vergence for the climatological winter and summer as we show in Figure 10, which ar-
 462 guably looks noisier than Figure 5a-d particularly north of the 300 m depth contour in
 463 the subpolar gyre.
 464

465 5 Discussion and summary

466 By running a 48-member ensemble run of the North Atlantic Ocean at mesoscale-
 467 permitting resolution ($1/12^\circ$), we have shown that the thickness-weighted average (TWA)
 468 framework can be employed successfully in diagnosing eddy-mean flow interactions in
 469 a realistic ocean simulation. In doing so, we have introduced a new buoyancy variable
 470 for a realistic EOS, which is neutral and dynamically consistent; both characteristics are
 471 necessary for the TWA analysis. The ensemble approach negates the necessity for any
 472 temporal averaging in defining the residual-mean flow; we are able to exclude any tem-

473 poral variability, such as seasonal and interannual fluctuations, from the eddy term and
 474 extract the intrinsic variability of the ocean. We show that the Eliassen-Palm (E-P) flux
 475 convergence (i.e. negative divergence), which encapsulates the eddy feedback onto the
 476 mean flow (Maddison & Marshall, 2013), tends to flux northward momentum to Gulf
 477 Stream on its northern flank and southward momentum on its southern flank ($-\bar{\mathbf{e}}_2 \cdot (\tilde{\nabla} \cdot$
 478 $\mathbf{E})$; Figure 5b,d,f,h); i.e. the eddies tend to smooth out the Gulf Stream in the merid-
 479 ional direction.

480 Modelling studies with varying spatial resolution have shown that the Gulf Stream
 481 tends to overshoot northwards and the North Atlantic Current (NAC) flows too zonally
 482 in coarse resolution models (e.g. Lévy et al., 2010; Chassignet & Xu, 2017, 2021). The
 483 overshooting may partially be attributable to eddy feedback being insufficiently resolved
 484 at mesoscale-permitting resolutions, in addition to unresolved submesoscale boundary
 485 layer processes (e.g. Renault et al., 2016). In particular, it would be interesting to see
 486 whether further increasing the model resolution would increase the amplitude of baro-
 487 clinic instability near the surface (E_b^{20}, E_b^{21}) and convergence of eddy momentum flux
 488 and potential energy in the interior (E_x^{00}, E_y^{11}), which tend to accelerate the jet south-
 489 ward in the subpolar gyre and decelerate it southward in the subtropical gyre upon the
 490 Gulf Stream separation west of 290°E (i.e. shift the jet southwards) as we see from their
 491 annual means (Figure 11). The same could be said for a better representation of the NAC
 492 path where the eddies in our model tend to flux northward momentum into the mean
 493 flow and hence allow for its north-eastward turn near the continental rise of the Grand
 494 Banks (Figures 4 and 5). Although it is beyond the scope of this study, the significance
 495 of baroclinic processes will likely increase with resolution as mixed-layer instability be-
 496 comes better resolved (Boccaletti et al., 2007; Capet et al., 2008a, 2008b; Su et al., 2018;
 497 Uchida et al., 2019; Yang et al., 2021).

498 We have also examined the often assumed ergodicity in decomposing the eddy and
 499 mean flow by replacing the averaging operator with a 50-year time mean for a single re-
 500 alization within the ensemble. To some extent, the agreement between Figures 4, 5, 11
 501 and 7 implies that the ensemble size of 48 is able to extract the eddy signals that emerge
 502 at mesoscale-permitting resolution. Amplitudes of the 95% confidence interval of the terms
 503 in E-P flux convergence being smaller than one-third of the amplitudes of the conver-
 504 gence itself supports the statistical significance of our eddy signals diagnosed from the
 505 ensemble (Figures 4 and C1). The difference between the ensemble and 50-year clima-

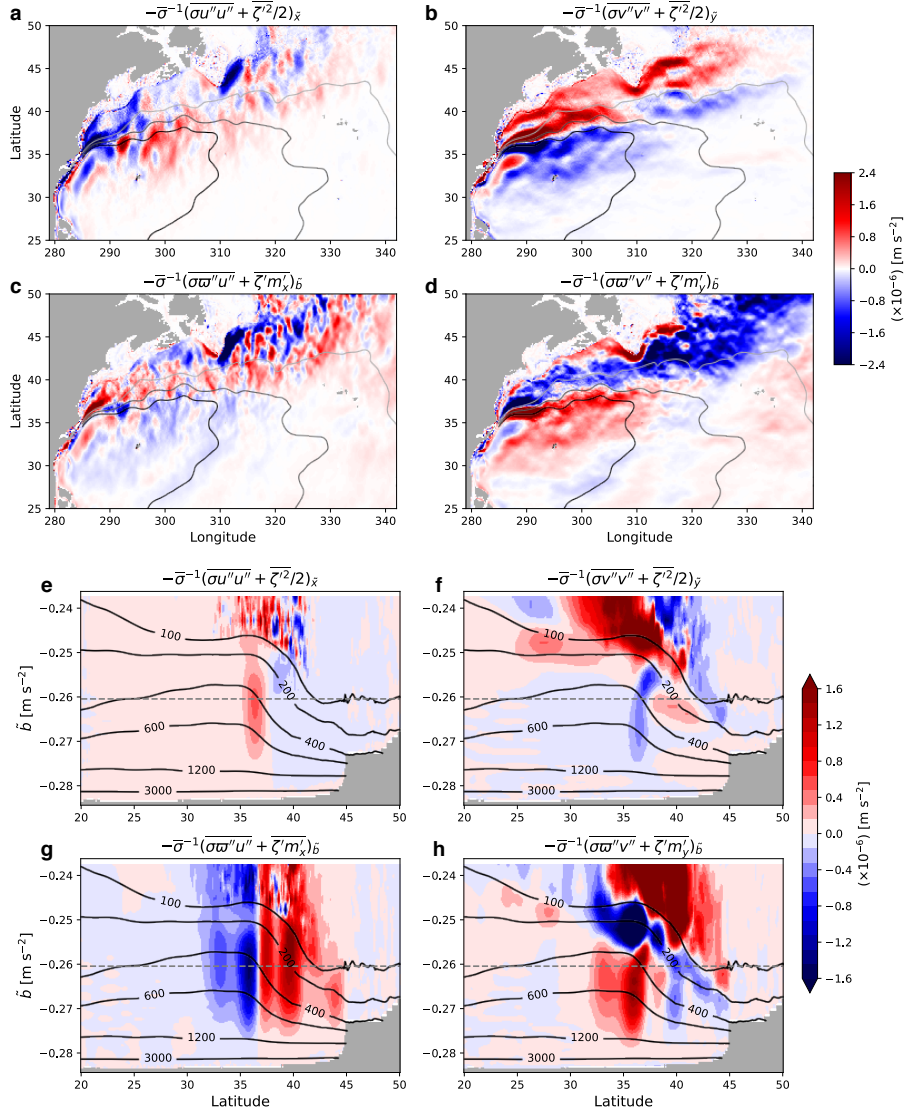


Figure 11. The annual mean of the convergence of eddy momentum flux and potential energy, and interfacial form stress for $\tilde{b} = -0.26$ **a-d**. The contours in grey shading east of 285°E indicate the 400, 300 and 200 m depth of the buoyancy surface. **e-h** The annual and zonal mean transect between 290°E-305°E of the E-P flux convergence is shown in colored shading and ensemble-mean depth in black contours. The iso-surface of buoyancy used through panels **a-d** is shown as the grey dashed line.

506 tology of an arbitrary realization amongst the ensemble (realization 00), on the other
 507 hand, likely comes from seasonal, interannual and decadal variability, and transient ed-
 508 dies, which are obscured in the climatological view. Loosening the time mean to a cli-
 509 matological annual cycle for the mean flow, on the other hand, convolutes the oceanic
 510 response to interannual variability in the atmospheric forcing and contaminates the eddy-
 511 mean flow decomposition (Figure 9). This is consistent with Aiki and Richards (2008)
 512 where they found the energy stored in the mean and eddy flow to change depending on
 513 the duration of the temporal averaging applied. While it is not our intention to claim
 514 whether defining the mean flow via a time mean is correct or not for realistic simulations,
 515 our results imply that one should be mindful of what goes into defining the mean flow
 516 and consequently the eddies.

517 Lastly, ensemble modelling has shown us that a small perturbation to the non-linear
 518 system can lead to very different states of the ocean and climate (e.g. Bessières et al.,
 519 2017; Maher et al., 2019; Jamet et al., 2019b; Uchida, Deremble, & Penduff, 2021; Fedele
 520 et al., 2021). In light of this, we argue that it is important to consider the full tempo-
 521 ral variability of the ocean and that eddy parametrizations should incorporate informa-
 522 tion of the time-varying eddy-mean flow interaction and not just its climatological state.

523 **Appendix A Energetics under a non-linear equation of state**

524 In this Appendix, we derive the energetics in a similar manner to Aiki et al. (2016)
 525 but in a framework consistent with the ensemble formalism and a realistic EOS. The TWA
 526 residual-mean horizontal momentum equation in geopotential coordinates neglecting dis-
 527 sipation is (Young, 2012; Ringler et al., 2017):

$$528 \quad \hat{\mathbf{u}}_t + \mathbf{v}^\# \cdot \nabla \hat{\mathbf{u}} + f \mathbf{k} \times \hat{\mathbf{u}} = -\nabla_h \phi^\# - \bar{\mathbf{e}} \cdot (\nabla \cdot \mathbf{E}), \quad (\text{A1})$$

529 where $\mathbf{v}^\# \stackrel{\text{def}}{=} \hat{u} \mathbf{i} + \hat{v} \mathbf{j} + w^\# \mathbf{k}$ and $\phi^\# \stackrel{\text{def}}{=} \bar{m}(\tilde{t}, \tilde{x}, \tilde{y}, b^\#(t, x, y, z)) + b^\# z$ are the residual-
 530 mean velocity and hydrostatic pressure anomaly. It is important to keep in mind that
 531 the “ z ” here is the ensemble averaged depth of an iso-surface of buoyancy, viz. $z = \bar{\zeta}(\tilde{t}, \tilde{x}, \tilde{y}, b^\#(t, x, y, z))$.
 532 The residual-mean kinetic energy (MKE; $K^\# = |\hat{\mathbf{u}}|^2/2$) budget becomes:

$$533 \quad K_t^\# + \mathbf{v}^\# \cdot \nabla K^\# = -\hat{\mathbf{u}} \cdot \nabla_h \phi^\# - \hat{\mathbf{u}} \cdot [\bar{\mathbf{e}} \cdot (\nabla \cdot \mathbf{E})] \quad (\text{A2})$$

$$534 \quad = -\hat{\mathbf{u}} \cdot \nabla_h \phi^\# - w^\# \phi_z^\# + w^\# b^\# - \hat{\mathbf{u}} \cdot [\bar{\mathbf{e}} \cdot (\nabla \cdot \mathbf{E})] \quad (\text{A3})$$

$$535 \quad = -\mathbf{v}^\# \cdot \nabla \phi^\# + w^\# b^\# - \hat{\mathbf{u}} \cdot [\bar{\mathbf{e}} \cdot (\nabla \cdot \mathbf{E})]. \quad (\text{A4})$$

536

537 We can now define the mean dynamic enthalpy as (McDougall, 2003; Young, 2010):

$$538 \quad h^\# \stackrel{\text{def}}{=} \int_{\Phi_0}^{\Phi^\#} \frac{b^\#(\bar{\theta}, \bar{s}, \Phi^\#)}{g} d\Phi^\# = \int_z^0 b^\# dz', \quad (\text{A5})$$

539 where $\Phi^\# = \Phi_0 - gz$ is the dynamically non-active part of the hydrostatic pressure to
 540 be consistent with the Boussinesq approximation. The material derivative of $h^\#(\bar{\theta}, \bar{s}, \Phi^\#)$
 541 is:

$$542 \quad \frac{D^\#}{Dt} h^\# = h_{\Phi^\#}^\# \frac{D^\# \Phi^\#}{Dt} + h_{\bar{\theta}}^\# \frac{D^\# \bar{\theta}}{Dt} + h_{\bar{s}}^\# \frac{D^\# \bar{s}}{Dt} \quad (\text{A6})$$

$$543 \quad = h_{\Phi^\#}^\# \Phi_z^\# \frac{D^\# z}{Dt} + h_{\bar{\theta}}^\# \frac{D^\# \bar{\theta}}{Dt} + h_{\bar{s}}^\# \frac{D^\# \bar{s}}{Dt} \quad (\text{A7})$$

$$544 \quad = -w^\# b^\# + h_{\bar{\theta}}^\# \frac{D^\# \bar{\theta}}{Dt} + h_{\bar{s}}^\# \frac{D^\# \bar{s}}{Dt}. \quad (\text{A8})$$

546 Therefore,

$$547 \quad \frac{D^\#}{Dt} (K^\# + h^\#) = -\nabla \cdot \mathbf{v}^\# \phi^\# + \mathcal{H}^\# - \hat{\mathbf{u}} \cdot [\bar{\mathbf{e}} \cdot (\nabla \cdot \mathbf{E})], \quad (\text{A9})$$

548 where $\mathcal{H}^\# \stackrel{\text{def}}{=} h_{\bar{\theta}}^\# \frac{D^\# \bar{\theta}}{Dt} + h_{\bar{s}}^\# \frac{D^\# \bar{s}}{Dt}$ and we have invoked $\nabla \cdot \mathbf{v}^\# = 0$.

549 On the other hand, the total KE budget remapped onto buoyancy coordinate is:

$$550 \quad \frac{DK}{Dt} = -\tilde{\nabla} \cdot \mathbf{v} \phi + w \tilde{b}, \quad (\text{A10})$$

551 where $\mathbf{v} \stackrel{\text{def}}{=} v^1 \mathbf{e}_1 + v^2 \mathbf{e}_2 + v^3 \mathbf{e}_3 = u \mathbf{e}_1 + v \mathbf{e}_2 + (\varpi + \frac{\zeta \hat{\mathbf{e}}}{\sigma}) \mathbf{e}_3$ and $\tilde{\nabla} \cdot \mathbf{v} = \sigma^{-1} [(\sigma v^1)_{\tilde{x}} +$
 552 $(\sigma v^2)_{\tilde{y}} + (\sigma v^3)_{\tilde{b}}] (= 0)$ is the three-dimensional divergence. Defining the dynamic en-
 553 thalpy in a similar manner as in equation (A5), namely,

$$554 \quad h = \int_{\zeta}^0 \tilde{b} d\zeta' = \int_{\tilde{b}}^{b_{\text{surf}}} b' \sigma db', \quad (\text{A11})$$

555 yields:

$$556 \quad \frac{D}{Dt} (K + h) = -\tilde{\nabla} \cdot \mathbf{v} \phi + \mathcal{H}, \quad (\text{A12})$$

557 where $\mathcal{H} \stackrel{\text{def}}{=} h_{\bar{\theta}} \frac{D\bar{\theta}}{Dt} + h_s \frac{Ds}{Dt}$. Ensemble averaging after thickness weighting equation (A12)

558 gives:

$$559 \quad \overline{\sigma \frac{D}{Dt} (K + h)} = -\overline{\sigma \tilde{\nabla} \cdot \mathbf{v} \phi} + \overline{\sigma \mathcal{H}} \quad (\text{A13})$$

$$560 \quad = -\overline{\sigma \widehat{\tilde{\nabla} \cdot \mathbf{v} \phi}} + \overline{\sigma \widehat{\mathcal{H}}}, \quad (\text{A14})$$

562 The total KE can be expanded as:

$$563 \quad K = \frac{1}{2} |\hat{\mathbf{u}} + \mathbf{u}''|^2 \quad (\text{A15})$$

$$564 \quad = \frac{|\hat{\mathbf{u}}|^2}{2} + \frac{|\mathbf{u}''|^2}{2} + \hat{u} u'' + \hat{v} v'' \quad (\text{A16})$$

$$565 \quad \stackrel{\text{def}}{=} K^\# + \mathcal{K} + \hat{u} u'' + \hat{v} v'', \quad (\text{A17})$$

599 potential energy at the TWA depth ($\hat{\zeta}$) and ensemble-mean depth ($\bar{\zeta}$). In a similar man-
 600 ner, we can also derive:

$$601 \quad h'' = -\tilde{b}(\zeta - \hat{\zeta}) = -\tilde{b}\zeta'', \quad (\text{A28})$$

602 and hence, $\widehat{h''} = -\widehat{\mathcal{H}}$. Assuming the background buoyancy frequency can be defined
 603 as the inverse of ensemble-mean thickness (viz. $\bar{\sigma}^{-1} \sim N^2$) leads to further manipu-
 604 lation of EPE:

$$605 \quad \widehat{\mathcal{H}} \sim -b^\# N^2 \overline{\zeta' \zeta'} = -b^\# N^2 \left(\frac{\overline{\zeta'^2}}{2} \right)_{\bar{b}} \quad (\text{A29})$$

$$606 \quad = -N^2 \left[\left(b^\# \frac{\overline{\zeta'^2}}{2} \right)_{\bar{b}} - \frac{\overline{\zeta'^2}}{2} \right], \quad (\text{A30})$$

608 where the last term in equation (A30) further reduces to the available potential energy
 609 under quasi-geostrophic approximation ($b' \sim N^2 \zeta'$). The first-term on the RHS of equa-
 610 tion (A30) vanishes upon volume integration pending on boundary conditions (i.e. rigid
 611 lid and a flat bottom).

612 **Appendix B Kinematics of discretization**

613 As in Figure B1, imagine u_1 and u_2 are on the same buoyancy contour. The re-
 614 lation between the two is:

$$615 \quad u_2 = u_1 + u_x \Delta x + u_\zeta \Delta \zeta. \quad (\text{B1})$$

616 Now,

$$617 \quad u_{\bar{x}} \stackrel{\text{def}}{=} u_x + \frac{\Delta \zeta}{\Delta x} \sigma^{-1} u_{\bar{b}} \quad (\text{B2})$$

$$618 \quad = u_x + \frac{\Delta \zeta}{\Delta x} u_\zeta \quad (\text{B3})$$

$$619 \quad = \frac{u_2 - u_1}{\Delta x} \quad (\because \text{equation (B1)}), \quad (\text{B4})$$

621 so once all of the variables are remapped onto the buoyancy coordinate from geopoten-
 622 tial, the discretized horizontal gradients can be taken along the original Cartesian grid.
 623 The gradients on the model outputs were taken using the `xgcm` Python package (Abernathey
 624 et al., 2021; Busecke & Abernathey, 2020). In order to minimize the computational cost,
 625 we took the ensemble mean first whenever possible, e.g. $\bar{\sigma} = \overline{\partial_b \zeta} = \partial_b \bar{\zeta}$, $\tilde{\nabla}_h \bar{\sigma} = \partial_b \tilde{\nabla}_h \bar{\zeta}$
 626 etc. The gradient operators commuting with the ensemble mean is also the case for the
 627 perturbations, i.e.

$$628 \quad \tilde{\nabla}_h (\bar{m} + m') = \tilde{\nabla}_h m = \overline{\tilde{\nabla}_h m} + (\tilde{\nabla}_h m)'. \quad (\text{B5})$$

629 Hence, $\tilde{\nabla}_h m' = (\tilde{\nabla}_h m)'$ (cf. Maddison & Marshall, 2013, Section 2.3 in their paper).

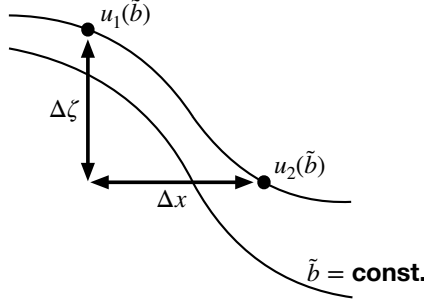


Figure B1. Schematic of discretized gradients.

630 **Appendix C Statistical significance of the eddy signals**

In this section, we examine the statistical significance of the terms in the E-P flux convergence. As the terms are all averaged quantities (e.g. $\bar{\sigma}E_{\tilde{y}}^{10} = [\overline{\sigma u''v''}]_{\tilde{y}}$), based on the Central-Limit Theorem, they should follow a Gaussian distribution. We can have an a-posteriori estimate of the standard deviation of the terms being averaged as (Menke & Menke, 2016):

$$\Sigma_{\text{post}}^{10} = \sqrt{\frac{1}{\mathcal{N}-1} \sum_{i=1}^{\mathcal{N}} ([\sigma u''v'']_{\tilde{y}_i} - [\overline{\sigma u''v''}]_{\tilde{y}})^2}, \quad (\text{C1})$$

where the subscript "post" indicates a-posteriori, and \mathcal{N} the number of ensembles. The 95% confidence interval of the E-P flux convergence terms becomes twice the root-mean square error (RSME):

$$RMSE = \frac{\Sigma_{\text{post}}}{\mathcal{N}-1}, \quad (\text{C2})$$

631 divided by the mean layer thickness (Figure C1). As the confidence interval is roughly
 632 one-third of the amplitudes of E-P flux convergence themselves, based on the Central-
 633 Limit Theorem, if we wanted reduce the uncertainty to 10%, we would need ~ 250 en-
 634 semble members.

635 **Acknowledgments**

636 This research was funded by the French ‘Make Our Planet Great Again’ (MOPGA) ini-
 637 tiative managed by the Agence Nationale de la Recherche under the Programme d’Investissement
 638 d’Avenir, with the reference ANR-18-MPGA-0002. High-performance computing resources
 639 on Cheyenne (doi:10.5065/D6RX99HX) used for running the ensembles were provided
 640 by NCAR’s Computational and Information Systems Laboratory, sponsored by the Na-
 641 tional Science Foundation, under the university large allocation UFSU0011. Dewar ac-
 642 knowledges support from the NSF grants OCE-1829856 and OCE-1941963. Balwada ac-

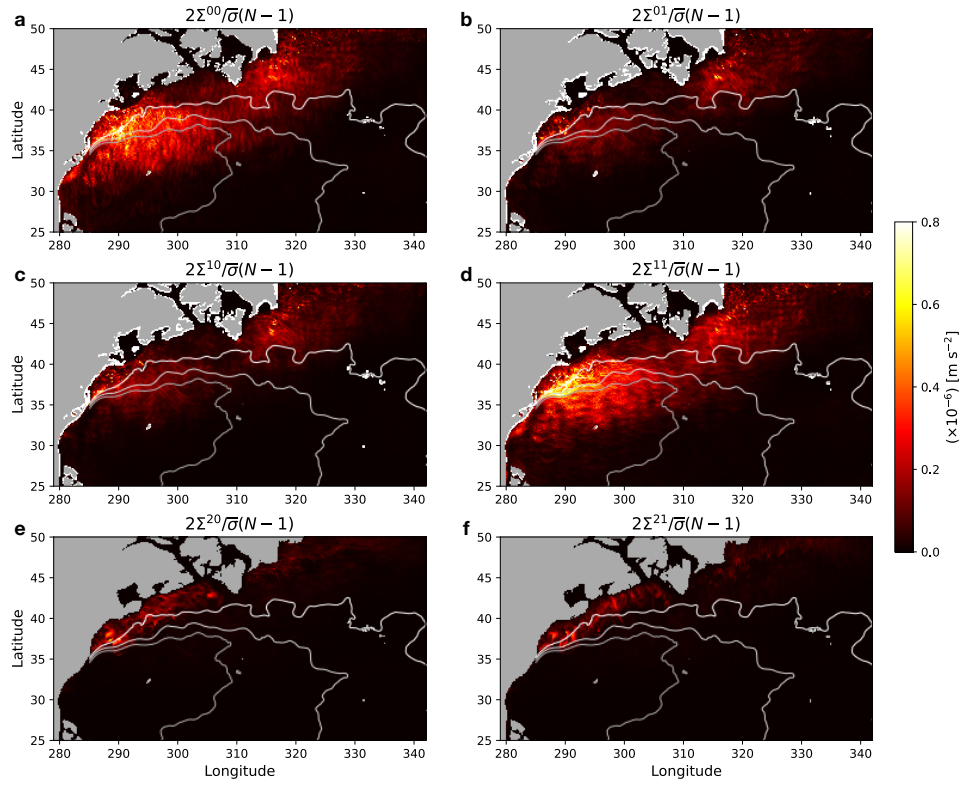


Figure C1. The 95% confidence interval of each term in the E-P flux convergence on January 3, 1967 on $\tilde{b} = -0.26 \text{ m}^2 \text{ s}^{-2}$. Σ^{ij} represents the a posteriori standard deviation of each term $\bar{\sigma}E_{\tilde{k}}^{ij}$ where the subscript \tilde{k} denotes the derivatives (equations 17 and 20).

643 knowledges support from the NSF grant OCE-1756882. We thank the editor Stephen
 644 Griffies, along with Laure Zanna and three other anonymous reviewers for their construc-
 645 tive and careful reviews, which lead to significant improvements in the manuscript. We
 646 would like to thank Geoffrey Stanley and Trevor McDougall for insightful discussions re-
 647 garding the buoyancy coordinate for a realistic EOS. The simulation outputs are avail-
 648 able on the Florida State University cluster ([http://ocean.fsu.edu/~qjamet/share/
 649 data/Uchida2021/](http://ocean.fsu.edu/~qjamet/share/data/Uchida2021/)). We also acknowledge Edward Peirce and Kelly Hirai for maintain-
 650 ing the cluster upon which the data analyses were conducted. Python scripts used for
 651 the off-line diagnosis are available on Github ([doi:10.5281/zenodo.4002824](https://doi.org/10.5281/zenodo.4002824)). Uchida
 652 acknowledges the `xarray` (Hoyer et al., 2021) and `dask` (Rocklin et al., 2021) Python
 653 package developers for parallelizing the analysis.

654 References

- 655 Abernathey, R. P. (2020). `fastjmd95`: Numba implementation of Jackett & Mc-
 656 Dougall (1995) ocean equation of state. Retrieved from [https://github.com/
 657 xgcm/fastjmd95](https://github.com/xgcm/fastjmd95)
- 658 Abernathey, R. P., Busecke, J., Smith, T., Banihirwe, A., Fernandes, F., Bourbeau,
 659 J., et al. (2021). `xgcm`: General circulation model postprocessing with `xar-
 660 ray`. Retrieved from <https://xgcm.readthedocs.io/en/latest/> doi:
 661 10.5281/zenodo.3634752
- 662 Aiki, H., & Richards, K. J. (2008). Energetics of the global ocean: the role of layer-
 663 thickness form drag. *Journal of Physical Oceanography*, *38*(9), 1845–1869. doi:
 664 10.1175/2008JPO3820.1
- 665 Aiki, H., Zhai, X., & Greatbatch, R. J. (2016). *Energetics of the global ocean: The
 666 role of mesoscale eddies*. World Scientific. doi: 10.1142/9789814696623_0004
- 667 Ajayi, A., Le Sommer, J., Chassignet, E., Molines, J.-M., Xu, X., Albert, A., &
 668 Cosme, E. (2020). Spatial and temporal variability of the north atlantic eddy
 669 field from two kilometeric-resolution ocean models. *Journal of Geophysical
 670 Research: Oceans*. doi: 10.1029/2019JC015827
- 671 Aluie, H., Hecht, M., & Vallis, G. K. (2018). Mapping the energy cascade in the
 672 north atlantic ocean: The coarse-graining approach. *Journal of Physical
 673 Oceanography*, *48*(2), 225–244. doi: 10.1175/JPO-D-17-0100.1
- 674 Andrews, D. G. (1983). A finite-amplitude Eliassen-Palm theorem in isentropic coor-
 675 dinates. *Journal of Atmospheric Sciences*, *40*(8), 1877–1883. doi: 10.1175/1520

- 676 -0469(1983)040(1877:AFAEPT)2.0.CO;2
- 677 Aoki, K. (2014). A constraint on the thickness-weighted average equation of motion
678 deduced from energetics. *Journal of Marine Research*, *72*(5), 355–382. doi: 10
679 .1357/002224014815469886
- 680 Aoki, K., Kubokawa, A., Furue, R., & Sasaki, H. (2016). Influence of eddy momen-
681 tum fluxes on the mean flow of the kuroshio extension in a 1/10 ocean general
682 circulation model. *Journal of Physical Oceanography*, *46*(9), 2769–2784. doi:
683 10.1175/JPO-D-16-0021.1
- 684 Arbic, B. K., Polzin, K. L., Scott, R. B., Richman, J. G., & Shriver, J. F. (2013).
685 On eddy viscosity, energy cascades, and the horizontal resolution of gridded
686 satellite altimeter products. *Journal of Physical Oceanography*, *43*(2), 283–300.
687 doi: 10.1175/JPO-D-11-0240.1
- 688 Bachman, S. D. (2019). The GM+E closure: A framework for coupling backscatter
689 with the Gent and McWilliams parameterization. *Ocean Modelling*, *136*, 85–
690 106. doi: 10.1016/j.ocemod.2019.02.006
- 691 Bachman, S. D., Anstey, J. A., & Zanna, L. (2018). The relationship between a
692 deformation-based eddy parameterization and the lans- α turbulence model.
693 *Ocean Modelling*, *126*, 56–62. doi: 10.1016/j.ocemod.2018.04.007
- 694 Bachman, S. D., Fox-Kemper, B., & Bryan, F. O. (2015). A tracer-based inver-
695 sion method for diagnosing eddy-induced diffusivity and advection. *Ocean*
696 *Modelling*, *86*, 1–14. doi: 10.1016/j.ocemod.2014.11.006
- 697 Balwada, D., Smith, S. K., & Abernathey, R. P. (2018). Submesoscale verti-
698 cal velocities enhance tracer subduction in an idealized antarctic circum-
699 polar current. *Geophysical Research Letters*, *45*(18), 9790–9802. doi:
700 10.1029/2018GL079244
- 701 Berloff, P. (2018). Dynamically consistent parameterization of mesoscale eddies.
702 Part III: Deterministic approach. *Ocean Modelling*, *127*, 1–15. doi: 10.1016/
703 j.ocemod.2018.04.009
- 704 Bessières, L., Leroux, S., Brankart, J.-M., Molines, J.-M., Moine, M.-P., Bouttier,
705 P.-A., ... Sérazin, G. (2017). Development of a probabilistic ocean modelling
706 system based on nemo 3.5: application at eddying resolution. *Geoscientific*
707 *Model Development*, *10*(3), 1091–1106. doi: 10.5194/gmd-10-1091-2017
- 708 Bire, S., & Wolfe, C. L. (2018). The role of eddies in buoyancy-driven eastern

- 709 boundary currents. *Journal of Physical Oceanography*, 48(12), 2829–2850. doi:
 710 10.1175/JPO-D-18-0040.1
- 711 Boccaletti, G., Ferrari, R., & Fox-Kemper, B. (2007). Mixed layer instabilities and
 712 restratification. *Journal of Physical Oceanography*, 37(9), 2228–2250.
- 713 Busecke, J., & Abernathey, R. P. (2020). CMIP6 without the interpolation: Grid-
 714 native analysis with pangeo in the cloud. In *Earthcube annual meeting*. Re-
 715 trieved from https://github.com/earthcube2020/ec20_busecke_etal
- 716 Capet, X., McWilliams, J. C., Molemaker, M. J., & Shchepetkin, A. F. (2008a).
 717 Mesoscale to submesoscale transition in the california current system. Part I:
 718 Flow structure, eddy flux, and observational tests. *Journal of physical oceanog-*
 719 *raphy*, 38(1), 29–43. doi: 10.1175/2007JPO3671.1
- 720 Capet, X., McWilliams, J. C., Molemaker, M. J., & Shchepetkin, A. F. (2008b).
 721 Mesoscale to submesoscale transition in the california current system. Part III:
 722 Energy balance and flux. *Journal of Physical Oceanography*, 38(10), 2256–
 723 2269. doi: <https://doi.org/10.1175/2008JPO3810.1>
- 724 Cessi, P., & Wolfe, C. L. (2013). Adiabatic eastern boundary currents. *Journal of*
 725 *Physical Oceanography*, 43(6), 1127–1149. doi: 10.1175/JPO-D-12-0211.1
- 726 Chassignet, E. P., & Xu, X. (2017). Impact of horizontal resolution ($1/12^\circ$ to
 727 $1/50^\circ$) on gulf stream separation, penetration, and variability. *Journal of*
 728 *Physical Oceanography*, 47(8), 1999–2021. doi: 10.1175/JPO-D-17-0031.1
- 729 Chassignet, E. P., & Xu, X. (2021). On the importance of high-resolution in large-
 730 scale ocean models. *Advances in Atmospheric Sciences*, 1–14. doi: 10.1007/
 731 s00376-021-0385-7
- 732 Cronin, M. (1996). Eddy-mean flow interaction in the gulf stream at 68 W. Part
 733 II: Eddy forcing on the time-mean flow. *Journal of Physical Oceanography*,
 734 26(10), 2132–2151. doi: 10.1175/1520-0485(1996)026<2132:EMFIIT>2.0.CO;2
- 735 de Boyer Montégut, C., Madec, G., Fischer, A. S., Lazar, A., & Iudicone, D. (2004).
 736 Mixed layer depth over the global ocean: An examination of profile data and a
 737 profile-based climatology. *Journal of Geophysical Research: Oceans*, 109(C12).
 738 doi: 10.1029/2004JC002378
- 739 Deremble, B., Wienders, N., & Dewar, W. (2013). CheapAML: A simple, at-
 740 mospheric boundary layer model for use in ocean-only model calculations.
 741 *Monthly weather review*, 141(2), 809–821. doi: 10.1175/MWR-D-11-00254.1

- 742 de Szoeké, R. A., & Bennett, A. F. (1993). Microstructure fluxes across density sur-
 743 faces. *Journal of Physical Oceanography*, *23*(10), 2254–2264. doi: 10.1175/1520
 744 -0485(1993)023(2254:MFADS)2.0.CO;2
- 745 de Szoeké, R. A., & Springer, S. R. (2009). The materiality and neutrality of neu-
 746 tral density and orthobaric density. *Journal of Physical Oceanography*, *39*(8),
 747 1779–1799. doi: 10.1175/2009JPO4042.1
- 748 Fairall, C. W., Bradley, E. F., Hare, J. E., Grachev, A. A., & Edson, J. B.
 749 (2003). Bulk parameterization of air–sea fluxes: Updates and verifica-
 750 tion for the coare algorithm. *Journal of climate*, *16*(4), 571–591. doi:
 751 10.1175/1520-0442(2003)016<0571:BPOASF>2.0.CO;2
- 752 Fedele, G., Penduff, T., Pierini, S., Alvarez-Castro, M. C., Bellucci, A., & Masina, S.
 753 (2021). Interannual to decadal variability of the kuroshio extension: analyzing
 754 an ensemble of global hindcasts from a dynamical system viewpoint. *Climate*
 755 *Dynamics*, 1–18. doi: 10.1007/s00382-021-05751-7
- 756 Fofonoff, N. (1981). *The gulf stream system. evolution of physical oceanography*. MIT
 757 Press. Retrieved from [https://ocw.mit.edu/ans7870/textbooks/Wunsch/
 758 Edited/Chapter4.pdf](https://ocw.mit.edu/ans7870/textbooks/Wunsch/Edited/Chapter4.pdf)
- 759 Gallimore, R. G., & Johnson, D. R. (1981). The forcing of the meridional circulation
 760 of the isentropic zonally averaged circumpolar vortex. *Journal of Atmospheric*
 761 *Sciences*, *38*(3), 583–599. doi: 10.1175/1520-0469(1981)038<0583:TFOTMC>2.0
 762 .CO;2
- 763 Greatbatch, R. J. (1998). Exploring the relationship between eddy-induced
 764 transport velocity, vertical momentum transfer, and the isopycnal flux of
 765 potential vorticity. *Journal of Physical Oceanography*, *28*(3), 422–432. doi:
 766 10.1175/1520-0485(1998)028<0422:ETRBEI>2.0.CO;2
- 767 Griffies, S. M., Winton, M., Anderson, W. G., Benson, R., Delworth, T. L., Dufour,
 768 C. O., ... others (2015). Impacts on ocean heat from transient mesoscale
 769 eddies in a hierarchy of climate models. *Journal of Climate*, *28*(3), 952–977.
 770 doi: 10.1175/JCLI-D-14-00353.1
- 771 Hoyer, S., Abernathey, R. P., Hamman, J., Bovy, B., Maussion, F., Fujii, K.,
 772 ... others (2021). *xarray: N-d labeled arrays and datasets*. Retrieved
 773 from <http://xarray.pydata.org/en/stable/index.html> doi: 10.5281/
 774 zenodo.598201

- 775 Jackett, D. R., & McDougall, T. J. (1995). Minimal adjustment of hydrographic pro-
 776 files to achieve static stability. *Journal of Atmospheric and Oceanic Technol-*
 777 *ogy*, *12*(2), 381–389. doi: 10.1175/1520-0426(1995)012<0381:MAOHPT>2.0.CO;
 778 2
- 779 Jackett, D. R., & McDougall, T. J. (1997). A neutral density variable for the world’s
 780 oceans. *Journal of Physical Oceanography*, *27*(2), 237–263. doi: 10.1175/1520
 781 -0485(1997)027<0237:ANDVFT>2.0.CO;2
- 782 Jamet, Q., Deremble, B., Wienders, N., Uchida, T., & Dewar, W. K. (2021). On
 783 wind-driven energetics of subtropical gyres. *Journal of Advances in Modelling*
 784 *Earth Systems*, e2020MS002329. doi: 10.1029/2020MS002329
- 785 Jamet, Q., Dewar, W. K., Wienders, N., & Deremble, B. (2019a). Fast warming
 786 of the surface ocean under a climatological scenario. *Geophysical Research Let-*
 787 *ters*, *46*(7), 3871–3879. doi: 10.1029/2019GL082336
- 788 Jamet, Q., Dewar, W. K., Wienders, N., & Deremble, B. (2019b). Spatiotemporal
 789 patterns of chaos in the atlantic overturning circulation. *Geophysical Research*
 790 *Letters*, *46*(13), 7509–7517. doi: 10.1029/2019GL082552
- 791 Jamet, Q., Dewar, W. K., Wienders, N., Deremble, B., Close, S., & Penduff, T.
 792 (2020). Locally and remotely forced subtropical amoc variability: A matter of
 793 time scales. *Journal of Climate*. doi: 10.1175/JCLI-D-19-0844.1
- 794 Jansen, M. F., Adcroft, A., Khani, S., & Kong, H. (2019). Toward an energetically
 795 consistent, resolution aware parameterization of ocean mesoscale eddies. *Jour-*
 796 *nal of Advances in Modeling Earth Systems*, *11*(8), 2844–2860. doi: 10.1029/
 797 2019MS001750
- 798 Jones, S. C., Busecke, J., Uchida, T., & Abernathey, R. P. (2020). Vertical re-
 799 gridding and remapping of CMIP6 ocean data in the cloud. In *Earthcube*
 800 *annual meeting*. Retrieved from [https://github.com/earthcube2020/
 801 ec20_jones_etal](https://github.com/earthcube2020/ec20_jones_etal)
- 802 Juricke, S., Danilov, S., Koldunov, N., Oliver, M., & Sidorenko, D. (2020). Ocean
 803 kinetic energy backscatter parametrization on unstructured grids: Impact on
 804 global eddy-permitting simulations. *Journal of Advances in Modeling Earth*
 805 *Systems*, *12*(1). doi: 10.1029/2019MS001855
- 806 Kitsios, V., Frederiksen, J. S., & Zidikheri, M. J. (2013). Scaling laws for pa-
 807 rameterisations of subgrid eddy–eddy interactions in simulations of oceanic

- 808 circulations. *Ocean Modelling*, *68*, 88–105. doi: 10.1016/j.ocemod.2013.05.001
- 809 Kjellsson, J., & Zanna, L. (2017). The impact of horizontal resolution on energy
810 transfers in global ocean models. *Fluids*, *2*(3), 45. doi: 10.3390/fluids2030045
- 811 Klocker, A., McDougall, T. J., & Jackett, D. R. (2009). A new method for forming
812 approximately neutral surfaces. *Ocean Science*, *5*(2), 155–172. doi: 10.5194/os
813 -5-155-2009
- 814 Lang, Y., Stanley, G. J., McDougall, T. J., & Barker, P. M. (2020). A pressure-
815 invariant neutral density variable for the world’s oceans. *Journal of Physical
816 Oceanography*, 1–58. doi: 10.1175/JPO-D-19-0321.1
- 817 Leroux, S., Penduff, T., Bessières, L., Molines, J.-M., Brankart, J.-M., Sérazin, G.,
818 ... Terray, L. (2018). Intrinsic and atmospherically forced variability of the
819 amoc: insights from a large-ensemble ocean hindcast. *Journal of Climate*,
820 *31*(3), 1183–1203. doi: 10.1175/JCLI-D-17-0168.1
- 821 Lévy, M., Klein, P., Tréguier, A.-M., Iovino, D., Madec, G., Masson, S., & Taka-
822 hashi, K. (2010). Modifications of gyre circulation by sub-mesoscale physics.
823 *Ocean Modelling*, *34*(1-2), 1–15. doi: 10.1016/j.ocemod.2010.04.001
- 824 Lévy, M., Resplandy, L., Klein, P., Capet, X., Iovino, D., & Éthé, C. (2012).
825 Grid degradation of submesoscale resolving ocean models: Benefits for of-
826 fine passive tracer transport. *Ocean Modelling*, *48*, 1–9. doi: 10.1016/
827 j.ocemod.2012.02.004
- 828 Maddison, J. R., & Marshall, D. P. (2013). The eliasen–palm flux tensor. *Journal
829 of Fluid Mechanics*, *729*, 69–102. doi: 10.1017/jfm.2013.259
- 830 Maher, N., Milinski, S., Suarez-Gutierrez, L., Botzet, M., Dobrynin, M., Kornbluh,
831 L., ... others (2019). The max planck institute grand ensemble: enabling the
832 exploration of climate system variability. *Journal of Advances in Modeling
833 Earth Systems*, *11*(7), 2050–2069. doi: 10.1029/2019MS001639
- 834 Marshall, D. P., Maddison, J. R., & Berloff, P. S. (2012). A framework for pa-
835 rameterizing eddy potential vorticity fluxes. *Journal of Physical Oceanography*,
836 *42*(4), 539–557. doi: 10.1175/JPO-D-11-048.1
- 837 Marshall, J., Hill, C., Perelman, L., & Adcroft, A. (1997). Hydrostatic, quasi-
838 hydrostatic, and nonhydrostatic ocean modeling. *Journal of Geophysical
839 Research: Oceans*, *102*(C3), 5733–5752. doi: 10.1029/96JC02776
- 840 McDougall, T. J. (2003). Potential enthalpy: A conservative oceanic variable for

- 841 evaluating heat content and heat fluxes. *Journal of Physical Oceanography*,
 842 33(5), 945–963. doi: 10.1175/1520-0485(2003)033<0945:PEACOV>2.0.CO;2
- 843 McDougall, T. J., & Jackett, D. R. (2005). An assessment of orthobaric density in
 844 the global ocean. *Journal of Physical Oceanography*, 35(11), 2054–2075. doi:
 845 10.1175/JPO2796.1
- 846 McDougall, T. J., & McIntosh, P. C. (2001). The temporal-residual-mean ve-
 847 locity. Part II: Isopycnal interpretation and the tracer and momentum
 848 equations. *Journal of Physical Oceanography*, 31(5), 1222–1246. doi:
 849 10.1175/1520-0485(2001)031<1222:TTRMVP>2.0.CO;2
- 850 Menke, W., & Menke, J. (2016). *Environmental data analysis with matlab* (2nd ed.).
 851 Academic Press.
- 852 Molines, J.-M., Barnier, B., Penduff, T., Treguier, A., & Le Sommer, J. (2014).
 853 ORCA12. L46 climatological and interannual simulations forced with DFS4.
 854 4: GJM02 and MJM88. drakkar group experiment rep. tech. rep. In *Gdri-*
 855 *drakkar-2014-03-19* (p. 50). Retrieved from [http://www.drakkar-ocean.eu/](http://www.drakkar-ocean.eu/publications/reports/orca12referenceexperiments2014)
 856 [publications/reports/orca12referenceexperiments2014](http://www.drakkar-ocean.eu/publications/reports/orca12referenceexperiments2014)
- 857 Montgomery, R. B. (1937). A suggested method for representing gradient flow in
 858 isentropic surfaces. *Bulletin of the American Meteorological Society*, 18(6-7),
 859 210–212. doi: 10.1175/1520-0477-18.6-7.210
- 860 Perezhogin, P. (2019). Deterministic and stochastic parameterizations of kinetic en-
 861 ergy backscatter in the nemo ocean model in double-gyre configuration. In *Iop*
 862 *conference series: Earth and environmental science* (Vol. 386, p. 012025). doi:
 863 10.1088/1755-1315/386/1/012025
- 864 Renault, L., Molemaker, M. J., Gula, J., Masson, S., & McWilliams, J. C. (2016).
 865 Control and stabilization of the gulf stream by oceanic current interaction with
 866 the atmosphere. *Journal of Physical Oceanography*, 46(11), 3439–3453. doi:
 867 10.1175/JPO-D-16-0115.1
- 868 Ringler, T., Saenz, J. A., Wolfram, P. J., & Van Roekel, L. (2017). A thickness-
 869 weighted average perspective of force balance in an idealized circumpo-
 870 lar current. *Journal of Physical Oceanography*, 47(2), 285–302. doi:
 871 10.1175/JPO-D-16-0096.1
- 872 Rocklin, M., Crist-Harif, J., Bourbeau, J., Augspurger, T., Durant, M., Signell, J.,
 873 ... others (2021). *dask: Parallel computing with task scheduling*. Retrieved

- 874 from <https://dask.org/>
- 875 Sasaki, H., Klein, P., Qiu, B., & Sasai, Y. (2014). Impact of oceanic-scale inter-
 876 actions on the seasonal modulation of ocean dynamics by the atmosphere. *Nature*
 877 *communications*, *5*(1), 1–8. doi: 10.1038/ncomms6636
- 878 Schubert, R., Jonathan, G., Greatbatch, R. J., Baschek, B., & Biastoch, A. (2020).
 879 The submesoscale kinetic energy cascade: Mesoscale absorption of subme-
 880 soscale mixed-layer eddies and frontal downscale fluxes. *Journal of Physical*
 881 *Oceanography*. doi: 10.1175/JPO-D-19-0311.1
- 882 Sérazin, G., Jaymond, A., Leroux, S., Penduff, T., Bessières, L., Llovel, W., ...
 883 Terray, L. (2017). A global probabilistic study of the ocean heat content low-
 884 frequency variability: Atmospheric forcing versus oceanic chaos. *Geophysical*
 885 *Research Letters*, *44*(11), 5580–5589. doi: 10.1002/2017GL073026
- 886 Stammer, D. (1997). Global characteristics of ocean variability estimated from re-
 887 gional topex/poseidon altimeter measurements. *Journal of Physical Oceanog-*
 888 *raphy*, *27*(8), 1743–1769. doi: 10.1175/1520-0485(1997)027<1743:GCOOVE>2.0
 889 .CO;2
- 890 Stanley, G. (2018). *Tales from topological oceans* (Doctoral dissertation, University
 891 of Oxford). Retrieved from [https://ora.ox.ac.uk/objects/uuid:414355e6](https://ora.ox.ac.uk/objects/uuid:414355e6-ba26-4004-bc71-51e4fa5fb1bb)
 892 [-ba26-4004-bc71-51e4fa5fb1bb](https://ora.ox.ac.uk/objects/uuid:414355e6-ba26-4004-bc71-51e4fa5fb1bb)
- 893 Stanley, G. J. (2019). Neutral surface topology. *Ocean Modelling*, *138*, 88–106. doi:
 894 10.1016/j.ocemod.2019.01.008
- 895 Su, Z., Wang, J., Klein, P., Thompson, A. F., & Menemenlis, D. (2018). Ocean sub-
 896 mesoscales as a key component of the global heat budget. *Nature communica-*
 897 *tions*, *9*(1), 775. doi: 10.1038/s41467-018-02983-w
- 898 Tailleux, R. (2016). Generalized patched potential density and thermodynamic
 899 neutral density: Two new physically based quasi-neutral density variables
 900 for ocean water masses analyses and circulation studies. *Journal of Physical*
 901 *Oceanography*, *46*(12), 3571–3584. doi: 10.1175/JPO-D-16-0072.1
- 902 Uchida, T., Abernathey, R. P., & Smith, S. K. (2017). Seasonality of eddy kinetic
 903 energy in an eddy permitting global climate model. *Ocean Modelling*, *118*, 41–
 904 58. doi: 10.1016/j.ocemod.2017.08.006
- 905 Uchida, T., Balwada, D., Abernathey, R. P., McKinley, G. A., Smith, S. K., & Lévy,
 906 M. (2019). The contribution of submesoscale over mesoscale eddy iron trans-

- 907 port in the open southern ocean. *Journal of Advances in Modeling Earth*
 908 *Systems*, 11, 3934–3958. doi: 10.1029/2019MS001805
- 909 Uchida, T., Deremble, B., Dewar, W. K., & Penduff, T. (2021). Diagnosing the
 910 Eliassen-Palm flux from a quasi-geostrophic double gyre ensemble. In *Earth-*
 911 *cube annual meeting*. Retrieved from [https://earthcube2021.github.io/](https://earthcube2021.github.io/ec21_book/notebooks/ec21_uchida_etal/notebooks/TU.05_Diagnosing-the-Eliassen-Palm-flux-from-a-quasi-geostrophic-double-gyre-ensemble.html)
 912 [ec21_book/notebooks/ec21_uchida_etal/notebooks/TU.05_Diagnosing-the](https://earthcube2021.github.io/ec21_book/notebooks/ec21_uchida_etal/notebooks/TU.05_Diagnosing-the-Eliassen-Palm-flux-from-a-quasi-geostrophic-double-gyre-ensemble.html)
 913 [-Eliassen-Palm-flux-from-a-quasi-geostrophic-double-gyre-ensemble](https://earthcube2021.github.io/ec21_book/notebooks/ec21_uchida_etal/notebooks/TU.05_Diagnosing-the-Eliassen-Palm-flux-from-a-quasi-geostrophic-double-gyre-ensemble.html)
 914 [.html](https://earthcube2021.github.io/ec21_book/notebooks/ec21_uchida_etal/notebooks/TU.05_Diagnosing-the-Eliassen-Palm-flux-from-a-quasi-geostrophic-double-gyre-ensemble.html) doi: 10.5281/zenodo.5496375
- 915 Uchida, T., Deremble, B., & Penduff, T. (2021). The seasonal variability of the
 916 ocean energy cycle from a quasi-geostrophic double gyre ensemble. *Fluids*,
 917 6(6), 206. doi: 10.3390/fluids6060206
- 918 Vallis, G. K. (2017). *Atmospheric and oceanic fluid dynamics* (2nd ed.). Cambridge
 919 University Press.
- 920 Waterman, S., & Lilly, J. M. (2015). Geometric decomposition of eddy feedbacks in
 921 barotropic systems. *Journal of Physical Oceanography*, 45(4), 1009–1024. doi:
 922 10.1175/JPO-D-14-0177.1
- 923 Xu, Y., & Fu, L.-L. (2011). Global variability of the wavenumber spectrum of
 924 oceanic mesoscale turbulence. *Journal of Physical Oceanography*, 41(4), 802–
 925 809. doi: <https://doi.org/10.1175/2010JPO4558.1>
- 926 Xu, Y., & Fu, L.-L. (2012). The effects of altimeter instrument noise on the esti-
 927 mation of the wavenumber spectrum of sea surface height. *Journal of Physical*
 928 *Oceanography*, 42(12), 2229–2233. doi: 10.1175/JPO-D-12-0106.1
- 929 Yang, P., Jing, Z., Sun, B., Wu, L., Qiu, B., Chang, P., & Ramachandran, S. (2021).
 930 On the upper-ocean vertical eddy heat transport in the kuroshio extension.
 931 Part I: Variability and dynamics. *Journal of Physical Oceanography*, 51(1),
 932 229–246. doi: 10.1175/JPO-D-20-0068.1
- 933 Young, W. R. (2010). Dynamic enthalpy, conservative temperature, and the seawater
 934 boussinesq approximation. *Journal of Physical Oceanography*, 40(2), 394–
 935 400. doi: 10.1175/2009JPO4294.1
- 936 Young, W. R. (2012). An exact thickness-weighted average formulation of the
 937 boussinesq equations. *Journal of Physical Oceanography*, 42(5), 692–707. doi:
 938 10.1175/JPO-D-11-0102.1
- 939 Zanna, L., & Bolton, T. (2020). Data-driven equation discovery of ocean

- 940 mesoscale closures. *Geophysical Research Letters*, e2020GL088376. doi:
941 10.1029/2020GL088376
- 942 Zanna, L., Mana, P. P., Anstey, J., David, T., & Bolton, T. (2017). Scale-aware
943 deterministic and stochastic parametrizations of eddy-mean flow interaction.
944 *Ocean Modelling*, 111, 66–80. doi: 10.1016/j.ocemod.2017.01.004
- 945 Zhao, K., & Marshall, D. P. (2020). Ocean eddy energy budget and parameteriza-
946 tion in the north atlantic. In *Ocean sciences meeting*. Retrieved from [https://](https://agu.confex.com/agu/osm20/meetingapp.cgi/Paper/646129)
947 agu.confex.com/agu/osm20/meetingapp.cgi/Paper/646129